



**HAL**  
open science

# Relating the physical properties of volcanic rocks to the characteristics of ash generated by experimental abrasion

Hannah Buckland, Julia Eychenne, Alison Rust, Katharine Cashman

► **To cite this version:**

Hannah Buckland, Julia Eychenne, Alison Rust, Katharine Cashman. Relating the physical properties of volcanic rocks to the characteristics of ash generated by experimental abrasion. *Journal of Volcanology and Geothermal Research*, 2018, 349, pp.335 - 350. 10.1016/j.jvolgeores.2017.11.017 . hal-01710672

**HAL Id: hal-01710672**

**<https://uca.hal.science/hal-01710672>**

Submitted on 14 Nov 2022

**HAL** is a multi-disciplinary open access archive for the deposit and dissemination of scientific research documents, whether they are published or not. The documents may come from teaching and research institutions in France or abroad, or from public or private research centers.

L'archive ouverte pluridisciplinaire **HAL**, est destinée au dépôt et à la diffusion de documents scientifiques de niveau recherche, publiés ou non, émanant des établissements d'enseignement et de recherche français ou étrangers, des laboratoires publics ou privés.



Distributed under a Creative Commons Attribution - NonCommercial - NoDerivatives 4.0 International License



Buckland, H. M., Eychenne, J., Rust, A. C., & Cashman, K. V. (2018). Relating the physical properties of volcanic rocks to the characteristics of ash generated by experimental abrasion. *Journal of Volcanology and Geothermal Research*, 349, 335-350.  
<https://doi.org/10.1016/j.jvolgeores.2017.11.017>

Peer reviewed version

Link to published version (if available):  
[10.1016/j.jvolgeores.2017.11.017](https://doi.org/10.1016/j.jvolgeores.2017.11.017)

[Link to publication record in Explore Bristol Research](#)  
PDF-document

This is the author accepted manuscript (AAM). The final published version (version of record) is available online via Science Direct at <http://www.sciencedirect.com/science/article/pii/S0377027317306832>. Please refer to any applicable terms of use of the publisher.

## University of Bristol - Explore Bristol Research

### General rights

This document is made available in accordance with publisher policies. Please cite only the published version using the reference above. Full terms of use are available:  
<http://www.bristol.ac.uk/red/research-policy/pure/user-guides/ebr-terms/>



13 **Abstract**

14 Interactions between clasts in pyroclastic density currents (PDCs) generate volcanic ash that can be  
15 dispersed to the atmosphere in co-PDC plumes, and due to its small size, is far-travelled. We designed  
16 a series of experiments to determine the effects of pyroclast vesicularity and crystal content on the  
17 efficiency and type of ash generated by abrasion. Two different pyroclastic materials were used: (1)  
18 basaltic-andesite pyroclasts from Fuego volcano (Guatemala) with ~26-46% vesicularity and high  
19 groundmass crystallinity and (2) tephri-phonolite Avellino pumice (Vesuvius, Italy) with ~55-75%  
20 vesicularity and low groundmass crystallinity.

21 When milled, both clast types produced bimodal grain size distributions with fine ash modes between  
22 4 and 5 $\phi$  (32-63 $\mu$ m). Although the vesicular Avellino pumice typically generated more ash than the  
23 denser Fuego pyroclasts, the ash-generating potential of a single pyroclast was independent of density,  
24 and instead governed by heterogeneous crystal and vesicle textures. One consequence of these  
25 heterogeneities was to cause the vesicular Avellino clasts to split in addition to abrading, which further  
26 enhanced abrasion efficiency. The matrix characteristics also affected ash shape and componentry,  
27 which will influence the elutriation and transport properties of ash in the atmosphere. The experimental  
28 abrasion successfully replicated some of the characteristics of natural co-PDC ash samples, as shown  
29 by similarities in the Adherence Factor, which measures the proportion of attached matrix on  
30 phenocrysts, of both the experimentally generated ash and natural co-PDC ash samples. Our results  
31 support previous studies, which have shown that abrasion is an effective mechanism for generating fine  
32 ash that is similar in size (~5 $\phi$ ; 30 $\mu$ m) to that found in co-PDC deposits. We further show that both the  
33 abundance and nature (shape, density, components, size distribution) of those ash particles are strongly  
34 controlled by the matrix properties of the abraded pyroclasts.

35 **Keywords**

36 Volcanic ash, abrasion, milling, shape, vesicularity, crystallinity

37

38

## 39 **1. Introduction**

40 Efficient fragmentation of bubbly melt into a dispersion of gas and pyroclasts can generate a large  
41 proportion of volcanic ash (Walker, 1981). Most commonly, the process is fuelled by magma  
42 overpressure, which generates the explosivity that transforms magma into pyroclasts, often with fractal  
43 size distributions (Rust and Cashman, 2011; Turcotte, 1986). Ash can also form, however, by  
44 ‘secondary fragmentation’ (Gonnermann, 2015) within the volcanic conduit (Dufek et al., 2012; Jones  
45 et al., 2016), in the thrust region of a volcanic plume (Cioni et al., 2014) or during transport in  
46 pyroclastic density currents (PDCs; Dufek and Manga, 2008; Eychenne et al., 2012).

47 Here we focus on secondary fragmentation in PDCs, where the energetic flow of gas and rock facilitates  
48 abrasion and comminution between clasts, as evidenced by the abundance of rounded pumice clasts in  
49 PDC deposits (e.g. Manga et al., 2011). These processes generate fine ash, which is important because  
50 it affects PDC runout (Dufek and Manga, 2008) and can become buoyant and form a co-PDC plume  
51 that disperses the fine fraction into the atmosphere (Engwell et al., 2016; Sparks et al., 1997). These  
52 ash particles are hazardous for human health and aviation (Gudmundsson et al., 2012; Horwell, 2007),  
53 and can add substantially to the fine ash fraction of the grain size distribution created by primary  
54 fragmentation; for this reason, it is important to anticipate the contribution of ash generated in PDCs to  
55 the total ash budget produced by an eruption. Previous studies show that the amount of ash generated  
56 by abrasion in PDCs will depend on a variety of factors such as the material in the PDC, the flow  
57 conditions and background eruptive behaviour (e.g., Gravina et al., 2004; Kueppers et al., 2012; Manga  
58 et al., 2011). Here we analyse the effects of pyroclast vesicularity and crystal content on the efficiency  
59 and type of ash generated by abrasion. We take an experimental approach, following previous studies  
60 that imitate abrasion in PDCs (Kueppers et al., 2012; Manga et al., 2011; Mueller et al., 2015). We  
61 extend these studies by using variably crystalline starting material and by quantifying the amount of ash  
62 generated, as well as the ash size, componentry and shape, as these parameters influence the particle  
63 settling behaviour and therefore both elutriation and transport potential in the atmosphere (Coltelli et  
64 al., 2008).

## 65 **2. Background**

66 Secondary fragmentation in PDCs has the potential to alter the total grain size distribution (TGSD) of  
67 an eruption (Rose and Durant, 2009). Specifically, the small mean grain size of co-PDC ash (typically  
68  $<63\ \mu\text{m}$ ; Engwell and Eychenne, 2016; Marti et al., 2016) increases the power law exponent of the grain  
69 size distribution (Jones et al., 2016). These small ash particles can travel long distances in the  
70 atmosphere (Engwell et al., 2014), such that co-PDC ash is often the furthest travelled ash from large  
71 ignimbrite-forming eruptions (Engwell and Eychenne, 2016). Consequently, understanding ash  
72 formation by secondary processes, such as abrasion in PDCs, is key for predicting the ash size  
73 distribution and ash dispersion potential of future PDC-generating eruptions.

74 The typically smooth shapes of pumice clasts in PDCs, regardless of distance of transport, indicate that  
75 clast rounding and, by inference, peak ash production, is rapid and takes place close to the vent (Manga  
76 et al., 2011). Experiments have replicated the rounding of pumice clasts observed in PDC deposits and  
77 the change in clast shape during abrasion has been related to the amount of ash generated in the flow  
78 (Dufek and Manga, 2008; Manga et al., 2011). Importantly, these experiments found that the maximum  
79 extent of clast rounding is not simply a function of the mass removed by abrasion. In fact, peak clast  
80 rounding can occur when clasts have lost between 15% and 60% of their initial mass. The broad range  
81 in the mass loss indicates that the peak ash production must be related, to some extent, to the properties  
82 of the abrading material.

83 The effect of clast vesicularity on the efficiency of ash generation has also been examined  
84 experimentally (Kueppers et al., 2012; Mueller et al., 2015), with low-density (vesicular) clasts  
85 generating more ash than denser (less vesicular) clasts when subjected to the same duration of milling  
86 in a rock tumbler. Here we suggest, however, that the differences in ash production are controlled not  
87 only by differences in vesicularity, but also by the crystal content (size, shape and abundance of  
88 phenocrysts and microlites). As PDC components from different volcanoes are extremely varied in  
89 both vesicularity and crystal content, both properties must be assessed to anticipate the ash-generating  
90 potential of a specific PDC.

91 Experiments have shown that the shape of ash is also altered by abrasion (Jones et al., 2016). In an  
92 experimental study using a ball mill, Jones et al. (2016) found that increased milling duration produced

93 ash particles with higher axial ratios (more equant shapes), which indicates the progressive rounding of  
94 ash grains, as well as increased removal of matrix from phenocrysts and phenocryst fragments (Freundt  
95 and Schmincke, 1992; Jones et al., 2016). From this perspective, it is possible that the shape and internal  
96 texture of ash generated by abrasion could be used to distinguish it from ash generated by the primary  
97 fragmentation of the magma. Field studies of the Lateral Volcanic Complex, Italy, have shown that  
98 sanidine crystals in the PDC deposit have fewer boundary irregularities than crystals of the same grain  
99 size in the fall deposit (Taddeucci and Palladino, 2002). Similarly, a preliminary assessment by Liu et  
100 al. (2015a) of Tambora ash suggests that co-PDC ash particles have grain boundaries with reduced  
101 roughness compared to fall-deposit ash of the same grain size.

102 The phenocryst content should also affect the efficiency of ash generation by abrasion, as crystals can  
103 influence fracture and breakage patterns in pyroclasts (Wawersik and Fairhurst, 1970). However, the  
104 effect of phenocrysts is not clear. Crystals may either resist erosional processes such as abrasion in mass  
105 flows, or conversely, may introduce planes of weakness, especially if they have platy textures or have  
106 been fractured by the initial brittle fragmentation (Bindeman, 2005; Thomson et al., 2013). For  
107 instance, experiments show that crystal-rich pyroclasts from Mount Unzen are more resistant to  
108 abrasion than less crystalline samples (Kueppers et al., 2012). Similarly, crystal-bearing Medicine Lake  
109 pumice abraded more slowly than crystal-free, texturally homogenous Taupo pumice of similar density  
110 (Manga et al., 2011). What still is unclear, however, is the effect of a heterogeneous distribution of  
111 phenocrysts and microlites, such as localised dense zones within a pumice clast, on the characteristics  
112 of ash generated by abrasion.

113 Also unexplored is the effect of groundmass crystallinity (i.e. microlite content) on the resistance of  
114 pyroclasts to abrasion. Hydrous mafic (basalt, basaltic andesite) magmas, in particular, experience  
115 extensive groundmass crystallization during rapid magma ascent in the conduit (e.g., Shea and Hammer,  
116 2013). The products of these eruptions also have total grain size distributions (TGSDs) with less fine  
117 ash than their microlite-free counterparts (Durant and Rose, 2009; Jones et al., 2016; Rust and Cashman,  
118 2011; Turcotte, 1986), which suggests that microlites affect primary fragmentation. We expect the role  
119 of groundmass crystallinity in secondary fragmentation processes to be four-fold. First, microlite-rich

120 samples also have low vesicularities, which would suggest that they should resist abrasion. Second,  
121 these samples have thick bubble walls, so that even if they abrade, the ash particles should be larger  
122 than in low crystallinity, high vesicularity samples. Third, analogue and numerical experiments  
123 (Oppenheimer et al., 2015; Parmigiani et al., 2016, 2011) show that groundmass crystals aid formation  
124 of gas pathways, which could control patterns of breakage. Finally, the crystal content of the resultant  
125 ash influences ash shape, as crystalline ash is typically blocky and lacks the perimeter concavities  
126 caused by abundant vesicles (Liu et al., 2015).

127 In this study, we test the efficiency of secondary ash generation by abrasion as a function of both  
128 vesicularity and crystallinity (phenocrysts and groundmass) of starting pyroclasts. We use samples  
129 from a violent Strombolian eruption of basaltic andesite Volcan Fuego, Guatemala, and from the Plinian  
130 Avellino eruption of tephra-phonolite from Vesuvius volcano, Italy. Informed by previous studies  
131 (Kueppers et al., 2012; Manga et al., 2011) we expected that the low density (high vesicularity) Avellino  
132 pumice would generate more ash than the high density (low vesicularity) Fuego pyroclasts. To test this  
133 hypothesis, we characterised the size, shape, vesicularity and crystallinity of the products both prior to  
134 and following abrasion experiments to dissect the links between the crystallinity, ash generation and  
135 ash shape. We then compare experimental and natural ash particles to assess the reliability of ash shape  
136 as an indicator of fragmentation process.

## 137 2.1 Volcan de Fuego (2012 eruption)

138 Volcan de Fuego is a stratovolcano located along the Central American volcanic arc in Guatemala. It  
139 produces frequent discrete violent Strombolian blasts with small ash plumes (<10km) and lava flows.  
140 Occasional ‘paroxysms’ of heightened activity generate Vulcanian to sub Plinian eruption columns and  
141 PDCs (Rose et al., 2008). The material used in our experiments is from a paroxysmal eruption in  
142 September 2012, which was more explosive than typical Strombolian activity (Chigna et al., 2012).  
143 The eruption produced a block and ash flow that we sampled ~6km from the vent on a field campaign  
144 in March 2016. The deposit is massive, poorly sorted and contains large blocks of basaltic andesite.  
145 We assume that the material is geochemically similar to basaltic-andesite explosive products from the



146 1974 eruption of Fuego (Chesner and Rose, 1984) as no geochemical analyses have been carried out on  
147 the 2012 eruptive products. This assumption is supported by the similarity of the phase assemblage to  
148 the 1974 material, and the lack of compositional differences between magma erupted in 1974, 1999 and  
149 2003 (Berlo et al., 2012). Major element analyses of the 1974 pyroclasts show an average silica content  
150 of 56.5 wt% and a total alkali content ( $\text{Na}_2\text{O} + \text{K}_2\text{O}$ ) of ~5.6 wt% (Chesner and Rose, 1984).

151 Additional material from Volcan de Fuego used in this study includes 2012 ash that was sampled from  
152 the top of a small block and ash flow. The ash represents the dilute portion of the PDC that settled out  
153 after the emplacement of the dense basal layer and is termed “PDC-surge” ash henceforth. The  $3\phi$   
154 (177-125 $\mu\text{m}$ ) fraction of this PDC-surge ash was imaged by E. Liu (*personal comm*). As a reference,  
155 we also analyse fall deposit ash generated during a paroxysm of Fuego in 2016 (sampled by E. Liu).

## 156 2.2 Pomici de Avellino (3.9ka B.P.)

157 An eruption of Somma-Vesuvius, Italy in 3.9ka B.P produced the Pomici de Avellino (PdA) deposit  
158 (Sulpizio et al., 2008). It was a large explosive eruption characterised by three distinct eruptive phases:  
159 an opening Plinian phase followed by a column collapse phase and a final phreatomagmatic phase  
160 (Sulpizio et al., 2010a). The stratigraphy is split into eruption units EU1 to 5 (Cioni et al., 1999). The  
161 products used in our experiments are from a PDC from EU3 that was generated during the column  
162 collapse phase. The PDC from this phase (EU3pf) was directed to the north, had a short runout (<10km)  
163 compared to the later EU5 PDCs (>20km, Sulpizio et al., 2010b) and is described as ‘poorly sorted  
164 massive to stratified lapilli and ash’ (Sulpizio et al., 2010b). Analyses of Avellino EU3 glasses by  
165 Sulpizio et al. (2010b) yield an average silica content of 55.6 wt% and a total alkali content of 12.8  
166 wt%, classifying the products as tephri-phonolite.

167 No distinct co-PDC or surge ash layer is found in the Avellino EU3 deposit (Sulpizio et al., 2010a).  
168 Instead, ash from the matrix of the dense part of the EU3pf deposit was sampled to compare to our  
169 experimentally generated ash and to examine the results of natural abrasion during transport in the flow.

170

## 171 **3. Methods**

### 172 **3.1. Characterisation of starting materials**

#### 173 3.1.1. Density

174 Juvenile clast densities were measured using the methodology of Houghton and Wilson (1989).  
175 Removable paraffin film of known density was used to seal the clasts for the density measurements  
176 which enabled clasts of known density to be later used in the abrasion experiments. The density  
177 distributions of the Fuego and Avellino clasts in the  $-3\phi$  (8-16mm) size range that we used as starting  
178 material are shown in Figure 1. The mean densities of the Fuego and Avellino pyroclasts are  $1.92 \text{ gcm}^{-3}$   
179  $^3$  and  $0.97 \text{ gcm}^{-3}$ , respectively. Each sample was divided into three sub-samples for the abrasion  
180 experiments (Fig. 1): one with a density close to the average of the bulk juveniles (AD), one with lower  
181 than mean density (LD) and the third with a higher than mean density (HD). This was done to test  
182 whether LD clasts (high vesicularity) generate more ash than the HD (low vesicularity) clasts. To track  
183 the change in shape of the large clasts (e.g., Manga et al., 2011), the clasts in each sub-sample were  
184 placed on a light board in order of ascending density and photographed before and after each abrasion  
185 experiment.

186 Dense rock equivalent (DRE) densities are required for calculating vesicularity. The Avellino DRE  
187 density used was  $2.42 \text{ gcm}^{-3}$  (Balcone-Boissard et al., 2012). The DRE density for Fuego was  
188 approximated from a dense juvenile, measured at  $2.79 \text{ gcm}^{-3}$  (Houghton and Wilson, 1989).

#### 189 3.1.2. Vesicularity

190 The vesicularity ' $V_D$ ' was calculated using the DRE densities of Avellino and Fuego lavas and the  
191 measured juvenile densities (e.g., Houghton and Wilson, 1989; Fig. 1). The average  $V_D$  calculated for  
192 Fuego was 31.2% and 59.6% for Avellino.

193 We also measured the vesicularity from polished thin sections of juvenile clasts ( $-3\phi$ ), as imaged using  
194 a Hitachi S-3500N Scanning Electron Microscope (SEM) at the University of Bristol in backscattered

195 electron (BSE) mode. Imaging the clasts at several magnifications ensured the optimum resolution for  
196 subsequent image analysis of both vesicles and crystals (Shea et al., 2010). Vesicularity and bubble  
197 number density (BND) were calculated from BSE images using FOAMS, a MATLAB™ based program  
198 (Shea et al., 2010) that converts 2D BSE images into a 3D representation of the vesicularity, ' $V_F$ '. The  
199 average vesicularity of four Fuego juvenile clasts was 32.4%, which is similar to the average measured  
200  $V_D$ . It was not possible to determine an accurate  $V_F$  for the EU3pf pumice using FOAMS because of the  
201 heterogeneity of the vesicle population. The measured  $V_F$  of pumice from the EU3 fall deposit is 56.1%  
202 (Voarino, 2016), which is similar to the  $V_D$  value of 59.6%. This, together with the close agreement of  
203  $V_D$  and  $V_F$  for Fuego, gives us confidence in the robustness of the density measurements.

### 204 3.1.3. Crystal Content

205 The phenocryst content of the starting materials was quantified using the BSE images acquired for  
206 vesicularity. Additional high magnification (1500x) BSE images were used to quantify the microlite  
207 content of the samples. Crystal identities were checked by energy dispersive spectroscopy (EDS) spot  
208 analyses on the SEM, after which the BSE grey scale value of each phase was used to map the phase  
209 distribution. The abundance of each phenocryst phase and the ratio of microlites to glass in the  
210 groundmass on a vesicle-free basis were determined with ImageJ.

## 211 3.2 Abrasion Experiments

212 The abrasion experiments were carried out using a planetary ball mill manufactured by Retsch Ltd. The  
213 Retsch Ltd PM 100 model has a vertical axis of rotation. This differs from studies in which a rock  
214 tumbler was used (Kueppers et al., 2012; Manga et al., 2011), where the rotation axis was horizontal.  
215 Typically, the Retsch planetary ball mill is used to generate very fine powders due to the milling  
216 efficiency that results from high centrifugal forces generated at high milling speeds (Mio et al., 2002).  
217 We did not want complete pulverisation of the samples, therefore short milling times were used (4-5  
218 mins). Additionally, the agate milling balls that encourage high energy impacts across the milling jar  
219 (Lu et al., 2012) were excluded, which means that the milling produces only clast-to-clast and clast-to-  
220 jar-wall interactions. We assume that friction at the jar walls is minimal due to the small mass of a

221 single clast and the smooth nature of the agate lined jar (Kueppers et al., 2012) and that the abrasion is  
222 driven mainly by clast interactions (both frictional sliding and impacts).

223 Sub-samples with an initial grain size of  $-3\phi$  (8-16mm) were used in the abrasion experiments. This  
224 ensured that all post-milling material smaller than the starting grain size was generated in the  
225 experiment. The number of clasts in each experiment was limited by the size of the grinding jar and  
226 the availability of material in the  $-3\phi$  fraction (Table 1). The grinding jar was sealed, placed on the  
227 rotating base and milled for 4 minutes with a rotation rate of 450 rpm (Fig. 2). Two additional Avellino  
228 abrasion experiments were carried out to investigate the effect of varying the starting grain size and the  
229 addition of a lithic component (sample Av31b and Av3AG, respectively; Table 1).

230 Our aim is to simulate processes occurring as clasts are transported in a PDC. The equivalent transport  
231 distance ( $x$ ) of the milling,

$$232 \quad x = l \cdot t \cdot v, \quad (1)$$

233 is  $\sim 425\text{m}$  for our experiments, with  $l$  being the inner milling jar circumference,  $t$  is the milling time in  
234 mins and  $v$  is the rotation rate in rpm (Kueppers et al., 2012). The speed at the wall of the rotating jar  
235 ( $= x / t$ ) was  $\sim 6.5\text{km/hr}$  which is an order of magnitude lower than typical PDC ground velocities (e.g.,  
236 Cole et al., 2002). However, the velocities of the clasts relative to each other during milling, are much  
237 higher due to the planetary ball mill configuration ( $>20\text{km/h}$ , Lu et al., 2012) and more comparable to  
238 the internal velocities in a natural PDC.

### 239 **3.3 Characterisation of experimental products**

#### 240 **3.3.1. Grain size distributions (GSDs)**

241 The milled samples were manually dry-sieved from  $-3$  to  $3\phi$  ( $\phi$ ), with half  $\phi$  sieving performed  
242 where possible. The size distribution of the fine material ( $>2\phi$ ,  $<250\mu\text{m}$ ) was quantified using a  
243 Mastersizer 3000™ by Malvern Instruments Ltd in the School of Geographical Sciences at the

244 University of Bristol. The fine and coarse fractions were combined to produce a GSD for each  
245 experiment using the overlap in the 3 $\phi$  size fraction (e.g., Jones et al., 2016).

### 246 3.3.2. Sample preparation and analysis conditions

247 After milling, grains from each size fraction were mounted and polished separately to ensure that all  
248 ash particles could be imaged at the same magnification (Liu et al., 2015a). When imaging the ash  
249 mounts, the objective was to balance the resolution of the images and the number of grains imaged.  
250 Typically, we found that at a working distance of  $\sim 15$ mm, an accelerating voltage of 15 or 20kV and  
251 200x magnification gave an optimum resolution ( $\sim 1560$  pixels/mm). Automated grid images, typically  
252 made up of 20-60 individual images, were stitched together using the ImageJ stitching plugin. The  
253 collated images contain 400-1000 grains with 30,000-60,000 pixels per grain. The ash componentry  
254 was then assessed from the BSE grid images with grains classified as free crystals, crystals with attached  
255 melt or matrix, groundmass grains, vesicular glass or pure glass.

### 256 3.3.3. Post-abrasion analysis of large clasts

257 The largest clasts (-3 and -2 $\phi$ ) remaining after the abrasion experiments were photographed and their  
258 size and shape compared with the original clasts of the same sub-sample. It was not possible to match  
259 each individual clast pre- and post-abrasion, therefore we amassed the shape data for all the sub-samples  
260 of each starting material and compared the average change in shape. We used the metric form factor  
261 'FF' (Liu et al., 2015; termed 'R' in Manga et al., 2011) to measure shape, where FF = 1 represents a  
262 perfect circle (Table 2):

$$263 \quad FF = 4\pi \cdot \text{area of particle} / (\text{perimeter of particle})^2. \quad (2)$$

264 The results of the shape analysis, particularly whether the FF increased (rounded) or decreased,  
265 informed our choice of which remaining clasts to mount for vesicularity and crystallinity  
266 characterization. As both starting materials were sampled from PDC deposits, the clasts had already  
267 experienced some degree of natural abrasion. The change in FF of the larger clasts from pre- to post-  
268 abrasion could therefore represent the effect of further transport in a natural flow.

269 3.3.4. Ash shape analysis

270 The BSE grid images gathered for componentry analysis were also used to measure particle shape.  
271 Images were first cleaned and converted to a binary form, then ash shape was measured using an ImageJ  
272 macro from Liu et al. (2015a). The natural ash samples from Fuego and Avellino (Table 1) were sieved,  
273 the 3 $\phi$  fraction imaged, and the cross-sectional shape measured using the same approach used for the  
274 experimentally generated ash. For comparison purposes, the resolution of the BSE images of the  
275 experimental ash was reduced to match the Fuego PDC-surge ash images (~390 pixels/mm, E. Liu,  
276 *personal comm.*), as convexity is sensitive to perimeter resolution. This was done by reducing the image  
277 size in ImageJ, which resamples the original image using bilinear interpolation (Ferreira and Rasband,  
278 2012). The image analysis and shape measurements were then repeated using the lower resolution  
279 images. Table 2 outlines the key shape parameters used in this study. Grains classified as ‘crystals with  
280 attached matrix’ in the componentry analysis were further analysed to determine the ‘Adherence Factor’  
281 (AF; Jones et al., 2016):

$$282 \quad AF = (\text{area of matrix}) / (\text{area of matrix} + \text{area of crystal}). \quad (3)$$

283 Values of AF close to 1 reflect a large proportion of attached matrix. This measurement required  
284 further manipulation of the BSE grid images to enhance the grey scale contrast between attached  
285 matrix and crystal.

286 The projected area of the experimental ash particles was measured using Morphologi G3SE™ by  
287 Malvern Instruments Ltd, an Optical Particle Analyser (OPA) located in the Laboratoire Magmas et  
288 Volcans, Clermont-Ferrand, France. Morphologi homogeneously disperses dry particles onto a glass  
289 plate using compressed air. The ash is then imaged and basic size and shape parameters of individual  
290 grains are measured using the same metrics in Table 2 (Leibrandt and Le Pennec, 2015). We analysed  
291 the 3 $\phi$  fraction of Fuego sample F3a and Avellino sample Av31a (Table 1) to compare with the results  
292 of the 2D shape analysis. The 4 $\phi$  (74-63  $\mu\text{m}$ ) fraction of these samples was also analysed to compare  
293 the shape measurements made across the two grain size fractions. The 4 $\phi$  fractions were sieved by

294 quarter phi increments, cleaned with ethanol and dried prior to analysis to ensure that very fine material  
295 was removed.

296 For each starting material and grain size, a standard operating procedure (SOP) was designed. The light  
297 source (diascopic or episcopic), magnification, focus, threshold and the area of the dispersion to scan  
298 were set manually (Leibrandt and Le Pennec, 2015). We concluded that the best resolution was  
299 provided by using a 5x optic with diascopic light (light from below) to obtain the 2D projected area of  
300 the ash shape. Once the SOP was defined, each analysis took 30-40 minutes depending on the scanning  
301 area.

302 Following the automated analysis, the Morphologi software (Malvern) generates an output file of the  
303 shape and grain size data. The 3 $\phi$  size fraction produced grain counts of 3000-7000, and the 4 $\phi$  analyses  
304 contained over 10 000 grains per sample. The output files required cleaning due to the imperfect nature  
305 of the imaging and automated dispersion (see Fig. S1). Grain counts in the 4 $\phi$  fraction were reduced to  
306 a sub-sample of 6000 randomly selected grains before the anomalous grains were removed. This  
307 ensured the same degree of manual error in the datasets of each grain size fraction.

## 308 **4. Results**

### 309 **4.1. Sample characterisation**

310 On a vesicle-free basis, Fuego pyroclasts have ~35% phenocrysts, but the phenocryst content ranges  
311 from 41% in a HD clast to 30% in a LD clast. The phenocrysts are dominantly plagioclase and olivine  
312 with sizes of 0.3-4mm. The average microlite content is ~40% in the groundmass (on vesicle-free basis)  
313 and comprises plagioclase (dominant), clinopyroxene, oxides and olivine. There is minor variability,  
314 but no significant difference in the microlite crystallinity between the high- and low-density sub-  
315 samples.

316 The vesicle size distribution (VSD) varies with density in the Fuego pyroclastic starting material. We  
317 prepared and imaged LD, AD (average density) and HD Fuego pyroclasts (Fig. 3) to analyse with  
318 FOAMS (Shea et al., 2010). There is a general trend of larger vesicle sizes and thicker bubble walls

319 with increasing density. The modal vesicle size of the HD clasts (Table 1) is  $1-0\phi$  (0.5-1mm), with no  
320 vesicles  $<5\phi$  (0.031mm) (Fig. 3d, h). LD clasts have a substantial fraction of bubbles (by area and by  
321 number)  $<2\phi$ mm (0.25mm) and a modal vesicle size between  $3-2\phi$  (Fig. 3a,b). Some LD clasts have a  
322 small number of large vesicles ( $>0\phi$ ) which account for a large area fraction (Fig. 3b, f). These clasts  
323 with large vesicles (Fig. 3b) also have more glomerocrysts and higher groundmass crystallinity than  
324 other LD clasts (Fig. 3a). From examining a small number of LD clasts (6), it appears the two types of  
325 LD textures (Fig. 3e, f) occur in equal proportion in the Fuego pyroclasts.

326 The average (vesicle-free) phenocryst crystallinity of the Avellino pyroclasts is  $\sim 12\%$ , ranging from  
327  $8\%$  in an LD pumice clast to a maximum of  $20\%$  in an HD pumice clast. The phenocrysts in the  
328 Avellino pumices are 0.2-1.5mm in size and dominantly sanidine and nepheline with minor amphibole,  
329 vesuvianite and clinopyroxene. The microlite content on a phenocryst and vesicle-free basis is 7-13%,  
330 and comprises sanidine, nepheline and minor skeletal leucites (Voarino, 2016). Spatial variations in  
331 microlite content include microlite-rich areas that are most frequent in the HD clasts (Fig. 4a and b).  
332 There are also fragments of thermally recrystallised limestone embedded in the pumice associated with  
333 large vesicles, which likely result from volatile release due to thermal decomposition of carbonate  
334 minerals (Fig. 4c, e.g. Jolis et al., 2015; Sottili et al., 2010). Leucite microlites and the dense microlite-  
335 rich areas appear to be unique to the dense mode of the EU3pf deposit (Voarino, 2016).

#### 336 **4.2. Grain size distributions**

337 All post-abrasion grain size distributions (GSDs) are bimodal, with most of the resultant ash  $\leq 125\mu\text{m}$   
338 ( $\geq 3\phi$ ; Fig. 5). Details of the GSDs differ, however, in that the fine mode lies at  $4\phi$  (63-90 $\mu\text{m}$ ) in the  
339 Fuego experiments and  $5\phi$  (32-45 $\mu\text{m}$ ) in the Avellino experiments. Moreover, the Avellino clasts  
340 generally produce more ash than the Fuego clasts. Cumulative grain size distributions for all experiments  
341 are shown in Figure 6, where the y-axis represents the starting grain size ( $-3\phi$ ). These distribution  
342 profiles highlight another consistent difference between Fuego and Avellino samples. The relatively  
343 flat profiles of the Fuego GSDs across the intermediate grain size fractions ( $-1$  to  $3\phi$ ) shows negligible  
344 formation of ash of intermediate size. In contrast, the Avellino GSDs do not have flat profiles between  
345  $-1$  and  $3\phi$ , meaning that milling generated particles across a wide range of grain sizes.



346 Overall, the Fuego milling experiments generated less ash than the Avellino experiments. In detail  
347 however, the response of individual Fuego pyroclasts to abrasion varies. The expected result was that  
348 the high density (low  $V_D$ ) sub-samples would generate the least ash and the low density (high  $V_D$ ) the  
349 most. For example, experiment F3a behaved as expected: >60% of the material generated in the LD  
350 experiment was smaller than  $-3\phi$ , whereas <16% of the material in the HD experiment was smaller than  
351  $-3\phi$ . However, most experiments did not show this behaviour: there are other Fuego experiments where  
352 LD sub-samples (highest  $V_D$ ), do not generate the highest proportion of ash (e.g., F2a; Fig. 5c).  
353 Similarly, the HD sub-samples, which contain clasts with high crystal contents (both phenocrysts and  
354 microlites) and low  $V_D$ , are not always the most resistant to abrasion.

355 Crystal-poor, high vesicularity Avellino experiments consistently have a smaller proportion of the  
356 material remaining in the  $-3\phi$  fraction than the experiments with crystal-rich, vesicle poor Fuego  
357 material. This indicates more efficient abrasion and ash generation for pyroclasts with low crystallinity  
358 and high vesicularity. We still see variability in the amount of ash generated, however. In one extreme,  
359 LD sub-sample Av31a yields <10% of mass remaining in the starting grain size, while milling of the  
360 AD (average density) sub-sample generated less ash (>40% of the material remaining in the starting  
361 size) than the HD sub-sample (Fig. 5d).

### 362 **4.3. Abrasion products**

#### 363 4.3.1. Shapes of large clasts

364 The median form factor (FF) of all large ( $-3$  and  $-2\phi$ ) clasts increased after milling (Fig. 7), reflecting  
365 the expected clast rounding due to abrasion (Manga et al., 2011). Although the median FF values  
366 increase, post-abrasion clast shapes are variable. At the same time, some experiments show an increase  
367 in the number of grains in the  $-3$  and  $-2\phi$  grain size fractions (see Table 1; Fig. 7). For example, milling  
368 of Av33a HD caused the number of large clasts to increase from 7 to 9. Both the range in FF values and  
369 the increase in particle number can be explained by splitting, rather than solely abrasion, of clasts.  
370 Splitting of clasts also explains the low (outlier) FF measurements in the Avellino data (Fig. 7) that  
371 indicate an increase in clast angularity.

#### 4.3.2. Projected area ash analysis from Morphologi

Ash shape measurements of the 3 $\phi$  AD sub-samples are shown in convexity (CVX) - solidity (SLD)-plots in Figure 8a, b (see Fig. S2 for 4 $\phi$  shape data). The shape data based on Morphologi images are concentrated at high-CVX and high-SLD values, as illustrated by the 20% contour of Fuego data, which plots between SLD values of 0.94-0.98 and CVX values of 0.95-0.98 for all the sub-samples. The same contour of the Avellino shape data plots between SLD and CVX values of  $\sim$ 0.95-0.98. In the extreme, however, the Avellino contour plots show a somewhat greater range, particularly in convexity. For example, the Avellino 90% contour extends to convexities of  $\sim$  0.87, whereas the Fuego 90% contour does not reach below CVX = 0.90.

Ash componentry was also evaluated using the Morphologi images, with categories designated as free crystal, vesicular, opaque (likely matrix dominated), crystal with attached melt or, in some cases, 'unknown'. The categorisation was done on a random selection of 500 grains per sample. The convexity and solidity values of these 500 grains are plotted in Figure 8c, d. The Fuego ash comprises mostly free crystals and opaque grains. The free crystals (red diamonds) typically record the highest SLD and CVX; opaque grains have a broader range in SLD and CVX. In the Avellino samples, vesicular grains (green asterisks) are numerous and plot with lower SLD and CVX values than the rest of the grains, reflecting the irregular outlines of these particles.

#### 4.3.3. Cross-sectional area (BSE) ash analysis

BSE images of polished 2D sections provide a more nuanced measure of particle shape as well as details of the internal textures of individual grains (Liu et al., 2015a). Again, we plot CVX vs. SLD of 3 $\phi$  grains from post-milling samples F3a and Av31a (Fig. 9). As anticipated, SLD and CVX measured on 2D images of cross-sections are much lower and more varied than the projected area (Morphologi) results. Note the more limited number of grains analysed (lower n values) compared to Figure 8 are because sample preparation and BSE image acquisition are more time consuming than Morphologi analyses. The Fuego ash ranges from 0.39-0.96 SLD and 0.50-0.95 CVX. The Avellino ash covers an even wider spectrum, with SLD ranging from 0.22 to 0.97 and CVX from 0.21-0.97.

398 Componentry analysis of the same particles (Fig. 10, Fig. S3) helps to explain the shape parameter  
399 range. Fuego ash is dominated by variably crystalline matrix fragments, with >50% of the grains being  
400 groundmass grains that have CVX and SLD values of ~0.75 – 0.9. Conversely, Avellino ash comprises  
401 predominantly free crystals and vesicular grains, the former having very high CVX and SLD values,  
402 and the latter marking the low CVX and SLD extremes.

403 The differences between the shape parameters measured by ImageJ and Morphologi reflect the  
404 differences between cross-sectional area and projected area (Liu et al., 2015a). Lower and more varied  
405 values of convexity and solidity are measured using BSE images and ImageJ due to the ability to  
406 measure small-scale roughness. The most extreme ash shapes measured by both methods (lowest values  
407 of CVX and SLD) are the vesicular grains that characterize the microlite-poor Avellino samples. The  
408 free crystals, in contrast, yield the highest SLD and CVX values (>0.95 in Fig. 8 and >0.8 in Fig. 9)  
409 using both methods, and thus provide an approximate measure of the free crystal content of individual  
410 ash samples.

#### 411 4.3.4 Natural ash samples

412 Two natural Fuego ash samples were analysed for their shape (Fig. 11a, b). The Fuego 2016 fall ash  
413 contains more grains with lower SLD and CVX values than the experimental or natural PDC-surge ash  
414 (Fig. 11). Similar to the experimental Fuego ash, the natural fall and surge ash show a range in microlite  
415 textures with an average microlite content of ~41%, comparable to the crystallinity measured from  
416 Fuego pyroclasts used in the experiments.

417 The CVX-SLD density plot of the natural PDC-surge and experimental Avellino ash (Fig. 11c) shows  
418 a slight increase in the number of low SLD and CVX values in the experimental ash compared to the  
419 natural ash. An important difference between the two samples is the presence of holocrystalline ash  
420 grains in the natural ash, which comprise ~29% of the components (Fig. 11f). They are the remnants  
421 of lithics that were incorporated into the Avellino PDC.

#### 422 4.3.5 Adherence Factor

423 Experimental ash from both Fuego and Avellino contained numerous ash grains that were classified as  
424 ‘crystals with attached matrix’ (Fig. 10). We quantified the amount of matrix attached to each imaged  
425 crystal in the  $3\phi$  size class using the ‘Adherence Factor’ (AF; Eq. 3). As shown in Figure 12, the  
426 Avellino and Fuego samples show contrasting AF distributions. Avellino ash samples yield the lowest  
427 AF values, whereas the Fuego samples, show a wide range of AF values. For comparison, we also  
428 include the results of milling experiments on Soufriere Hills Volcano (SHV) pumice (Jones et al., 2016)  
429 which has intermediate values of vesicularity and crystallinity, and correspondingly intermediate AF  
430 trends.

## 431 **5. Discussion**

432 The abrasion experiments show that, for the same duration of milling, the Avellino pumice generated  
433 more ash than the denser Fuego juvenile material (Figs. 5 and 6). This supports the results of Kueppers  
434 et al. (2012), who found that material of lower density and higher vesicularity generates more ash when  
435 abraded. However, the results are less straightforward when the starting material is examined in the  
436 context of density-designated sub-samples from the same eruption. This means that density alone  
437 cannot be used to predict the behaviour of material subjected to abrasion. Moreover, our experiments  
438 show that ash shape, size and componentry vary both within and between samples. As these parameters  
439 determine the transport properties of secondary ash particles, understanding controls on these properties  
440 is critical for predicting the contributions of co-PDC ash to distal ash clouds.

### 441 **5.1 Effects of pyroclast textural heterogeneity on abrasion**

#### 442 5.1.1 Fuego pyroclasts

443 The vesicle size distribution (VSD) of pyroclasts influences the TGSD generated by primary  
444 fragmentation (Liu et al., 2015b; Rust and Cashman, 2011). The VSD of pyroclasts may also affect the  
445 extent of secondary fragmentation because vesicles affect brittle rock strength (Heap et al., 2014) and  
446 form zones of weakness that may control patterns of breakage. Sub-samples in the Fuego experiments,  
447 in particular, display a wide range in the amount of ash generated, which likely reflects VSD variations  
448 in the Fuego starting material (Fig. 3). If clasts abrade by fracturing at the weakest point, which

449 typically will be the thinnest part of a vesicle wall, then the low vesicle number density and increased  
450 thickness of the bubble walls in the HD samples explains the resistance to abrasion of the HD clasts.  
451 The average bubble wall thickness may also control the size of the abraded ash particles (typically  $4\phi$ ,  
452 or  $\sim 63 \mu\text{m}$ , in Fuego LD samples).

453 Not all Fuego LD clasts generated a large proportion of ash when abraded (Fig. 5c), however. To  
454 address this discrepancy, we imaged two post-milling LD clasts of similar density: one that recorded a  
455 25% decrease in projected area with visible rounding (Fig. 3a) and one that recorded only a 2% decrease  
456 in projected area and showed a decrease in FF post-milling, rather than the expected increase (Fig. 3b).  
457 The clast that did not round (Fig. 3b) has a smaller modal vesicle size, elevated microlite crystallinity  
458 and a greater number of phenocrysts, glomerocrysts and large vesicles compared to the LD clast that  
459 did round (Fig. 3a). Here the few large vesicles ( $\sim 0.5\text{mm}$ ; Fig. 3b) allow the non-rounded clast to retain  
460 a low density, whilst the high crystallinity (both glomerocrysts and microlites) controls its resistance to  
461 abrasion. It seems likely that the relative proportions of these two clast types in the LD sub-samples  
462 explains the range in ash production rates. The importance of heterogeneities in ash generation means  
463 that our individual experiments with a small number of clasts are not representative; however, the  
464 limited set of clasts allows us to explore the differences in sub-samples by isolating individual clasts,  
465 monitoring their behaviour post-milling and attributing differences in behaviour to differences in  
466 vesicularity and crystal content.

#### 467 5.1.2 Avellino pyroclasts

468 The Avellino experiments consistently generated a higher proportion of ash than the experiments with  
469 denser Fuego pyroclasts. Interestingly, however, the HD sub-samples generated more ash than the AD  
470 sub-samples in two of the Avellino experiments, contrary to the expectation that high density (low  
471 vesicularity) clasts would be most resistant to abrasion (Kueppers et al., 2012). Sectioning of selected  
472 clasts shows that the EU3pf pumice is highly heterogeneous in both vesicularity and crystal content,  
473 particularly in the HD clasts. For example, HD clasts can contain microlite-rich zones that have a high  
474 number density of microlites and low vesicularity relative to the surrounding melt (Fig. 4a, b; Voarino,

475 2016), textural features that should make these zones relatively resistant to abrasion, leading us to  
476 further question the high proportion of ash generated by two of the HD sub-samples.

477 The  $-2\phi$  fraction of the EU3pf deposit has a bimodal density distribution, unlike the  $-3\phi$  fraction, with  
478 a secondary dense mode created by clasts with relatively high microlite content (Voarino, 2016). To  
479 test the response to abrasion of microlite-rich clasts, we carried out an additional abrasion experiment  
480 using the dense Avellino pumices from the  $-2\phi$  fraction (sample Av31b in Table 1). The resulting GSD  
481 (Fig. 6c) shows that the clasts were less abraded than the  $-3\phi$  clasts even when milled for an extra  
482 minute, confirming that the increased microlite content of the  $-2\phi$  strongly enhances their resistance to  
483 abrasion. However, the extremely microlite-rich zones (Fig. 4), were only present in two out of five HD  
484 clasts imaged post-abrasion. Therefore, rather than limiting abrasion, the HD clasts which have  
485 elevated microlite content or contain dense zones could increase abrasion by acting as resistant grains  
486 that abrade the more vesicular clasts. This is analogous to the scenario where a lithic component (i.e.  
487 more resistant lithology) incorporated in PDCs encourages efficient abrasion (Bernard and Le Pennec,  
488 2016). This may be one explanation for the unexpected behaviour of some HD subsamples (Fig. 5,6).

489 Additional heterogeneities in Avellino clasts include xenoliths of altered limestone, which generate  
490 cavities in the surrounding melt by decarbonation (Fig. 4c). These cavities introduce internal  
491 weaknesses that may promote clast splitting rather than abrasion (see section 5.2).

492 The heterogeneities observed within the Fuego and Avellino pyroclasts are typical of the textural  
493 heterogeneity found in natural PDC material (e.g. Bernard and Le Pennec, 2016; Gardner et al., 1998).  
494 Importantly we have shown that textural heterogeneity within a density class from a single eruption can  
495 influence pyroclast resistance to abrasion. The demonstrated sensitivity of clast abrasion to internal  
496 heterogeneities means that density alone cannot be used to predict the efficiency of ash production by  
497 abrasion within a PDC.

## 498 **5.2 Enhanced ash production due to clast splitting**

499 The increase in the post-milling clast count in the  $-2\phi$  and  $-3\phi$  fractions (Table 1) indicates that some  
500 clasts split during the abrasion experiments. Clast splitting can facilitate further abrasion, as it increases

501 the total surface area and number of sharp corners that control abrasion (Manga et al., 2011). The  
502 Avellino experiments showed the most evidence for splitting during milling, with the clast number  
503 almost doubling (from 7 to 12 clasts) in one sub-sample (Av32a AD sample; Table 1). In these  
504 experiments, the large proportion of material in the  $-2\phi$  grain size (expected for splitting of  $-3\phi$  grains),  
505 as well as the abundance of ash in the intermediate grainsizes ( $-1\phi$  to  $2\phi$ ; Fig. 5), suggest that splitting  
506 was a dominant, rather than occasional, process. The post-abrasion range in FF values and the  
507 frequency of outlying FF values (Fig. 7) also provide evidence of splitting. The HD sub-sample of  
508 Av33a provides a particularly striking example of the hypothesis that splitting of Avellino clasts aids  
509 efficient ash generation. Here the largest clast completely disintegrated (extensive splitting), which  
510 increased ash generation across the intermediate ( $-1\phi$  to  $2\phi$ ) grain sizes compared to the other Avellino  
511 HD subsamples (Fig. 6b).

512 Our data further suggest that internal weaknesses that encourage splitting (such as large vesicles or  
513 cavities formed by decarbonation) are exploited rapidly, so that over time, splitting becomes far less  
514 common. This means that after long milling times (as in Manga et al., 2011), rounding of all fragments  
515 makes the products of splitting indistinguishable from clasts that experienced only abrasion. If we had  
516 used longer milling times for our experiments, the effects of splitting may have been masked by  
517 continual abrasion of the split clasts. In a natural setting, initial splitting of clasts may add to the early  
518 maximum in ash production by comminution between clasts as the splitting exposes rough surfaces that  
519 are readily available for progressive abrasion (Dufek and Manga, 2008).

### 520 **5.3 Enhanced ash production due to the interaction of pyroclasts with variable resistance**

521 A recent study of PDC deposits from Tungurahua volcano in Ecuador (Bernard and Le Penneç, 2016)  
522 found that old lava clasts incorporated within the flow caused early splitting of pristine juvenile  
523 components (termed ‘grinding’), due to the increased strength of the lava. This interpretation is  
524 supported by our supplementary Avellino experiment, Av3AG (Table 1). Here adding an agate ball to  
525 the grinding jar (analogous to adding a resistant lithology) enhanced ash production, particularly in the  
526 intermediate grain size fractions (Fig. 6c). The study of the Tungurahua PDC deposits further indicates  
527 that initial splitting (or ‘grinding’) of the juvenile clasts generates a ‘milling factory’ that produces small

528 juvenile fragments that are available to abrade (Bernard and Le Pennec, 2016). This is consistent with  
529 our results showing that initial breakage of clasts ( $-3$  or  $-2\phi$ ) will enhance further ash production by  
530 abrasion (see section 5.2).

531 Taken together, these observations suggest that the presence (in PDCs) of mixed lithologies with  
532 different strengths encourages a productive milling factory, making block-and-ash flows prone to ash  
533 production. Large volume PDCs (ignimbrites), in contrast, tend to be pumice-dominated, with minor  
534 contributions of lithic fragments (e.g., Sparks et al., 1973). Therefore, enhanced splitting and abrasion  
535 due to grinding by a resistant lithic component could be less important in pumice-dominated flows than  
536 in flows with a higher lithic content. Our experiments also suggest, however, that even a small  
537 proportion of lithics will enhance ash production.

#### 538 **5.4 Controls of the starting materials texture on the characteristics of the ash produced**

##### 539 5.4.1 Ash grainsize

540 The fine modes of GSDs produced by abrasion experiments are  $5\phi$  for Avellino and  $4\phi$  for Fuego. The  
541 difference in the fine modes reflects the different starting materials used. Thin vesicle walls provide  
542 preferential places for rocks to fracture (e.g., Heap et al., 2014). If abrasion is caused by breakage of  
543 juvenile clasts at vesicle walls, the size of the ash generated will be limited by the bubble wall thickness,  
544 which explains the coarser mode ( $4\phi$ ) of the ash generated by the (thick walled) Fuego experiments.  
545 Fracturing and breakage of volcanic rocks can also occur in the absence of vesicles. In this case it is  
546 likely that the high crystallinity ( $\sim 40\%$ ) of the Fuego groundmass will prevent extensive breakage of  
547 particles into smaller grainsizes as microlites likely increase the strength of the groundmass (Heap et  
548 al., 2016).

##### 549 5.4.2 Ash componentry

550 The experimental GSDs show that the crystallinity and vesicularity of the starting material exert strong  
551 controls on the amount and size of ash generated by abrasion. The starting material properties also  
552 strongly influence the physical attributes of the resulting ash. For example, the abundance of vesicular  
553 ash grains is controlled by the minimum vesicle size in the starting material (Liu et al., 2015b). For this



554 reason, the Fuego 3 $\phi$  (175-125  $\mu\text{m}$ ) ash lacks vesicular grains because the dominant vesicle size in  
555 Fuego clasts is  $>100\mu\text{m}$  in diameter (Figs. 3 and 10). Avellino ash of the same grain size, in contrast,  
556 contains a high proportion of vesicular grains because the average vesicle size in the pumice is smaller  
557 than the ash size (Fig. 10).

558 The crystal content of the ash reflects the crystallinity of the starting materials. The Fuego 3 $\phi$  ash  
559 comprises  $>90\%$  crystalline particles (free crystals and crystal-rich groundmass) compared to  $\sim 70\%$   
560 crystalline particles in the Avellino 3 $\phi$  ash (mostly phenocrysts with or without attached matrix).  
561 However, the proportion of free crystals in the Avellino ash is higher than in the Fuego ash. This could  
562 be the result of efficient liberation of crystals from the surrounding matrix during abrasion (Fig. 12)  
563 and/or breakage of larger crystals along cleavage planes (Jones et al., 2016). Without analysing ash  
564 componentry in other grain size fractions, however, it is not possible to determine the primary origin of  
565 the free crystal fragments or the abundance of free crystals in the whole ash sample.

566 Experimental milling (abrasion) can also reduce the amount of matrix adhered to crystals (the  
567 Adherence Factor, AF) of ash particles (Jones et al., 2016). The Adherence Factor trends shown in  
568 Figure 12 clearly distinguish the Fuego ash (higher proportion of high AF) from the Avellino ash  
569 (mostly low AF values). The different AF trends reflect different textures in the starting material, most  
570 importantly, the vesicularity of the matrix surrounding the crystals. For example, the low vesicularity  
571 and thick bubble walls in the Fuego clasts (Fig. 3) means the maximum amount of matrix that can be  
572 attached to a crystalline ash particle is greater than for the Avellino pumice, thus explaining the higher  
573 AF values. Another factor that could influence the AF is the variable thermal contraction of  
574 components during cooling which can create curvilinear fractures separating crystals from the glass  
575 (Andronico and Cioni, 2002). These fractures would help liberate crystals from the melt increasing the  
576 occurrence of crystals with a minor amount of attached matrix and therefore a low AF.

#### 577 5.4.3 Ash Shape

578 It has been suggested that co-PDC ash might have more uniform shapes than fall ash due to the  
579 smoothing of grain boundaries by abrasion (Liu et al., 2015a; Taddeucci and Palladino, 2002). This was

580 illustrated by Tambora co-PDC ash, which had a higher convexity (CVX) than fall ash with the same  
581 solidity (SLD), consistent with an abrasion-induced decrease of the roughness of grain perimeters  
582 during transport within PDCs (Liu et al., 2015a). The analysis was based, however, on a limited number  
583 of 2 $\phi$  (350-500 $\mu$ m) ash particles (Maria and Carey, 2007). Here we assess the extent to which fine-  
584 grained ash generated by experimental abrasion records similarly high convexity values as the result of  
585 rounding.

586 The highest density of data points for both Avellino and Fuego ash (the 50% contour encloses  
587 approximately half of the data) plot with CVX and SLD >0.9 (Fig. 8). However, the Avellino projected  
588 area shape analysis extends to lower CVX and SLD values (~0.87) than for Fuego ash (~0.9). This  
589 difference reflects the componentry, with the vesicular grains in the Avellino ash having low CVX and  
590 SLD. The different SLD and CVX ranges for Avellino and Fuego ash are more pronounced in the  
591 cross-sectional shape analysis, shown in Figure 9. This demonstrates the ability of this method to  
592 distinguish particles characterised by contrasting internal structures rather than using the projected  
593 shape (Morphologi). We therefore conclude that not all ash formed by abrasion will record high  
594 convexity values, particularly when grains are vesicular. These data also show that the morphological  
595 changes undergone by lapilli and ash can be decoupled during milling in PDCs, with larger clasts  
596 rounding but newly generated ash having highly irregular shapes. This is particularly apparent in the  
597 Avellino experiments where lapilli clasts exhibit pronounced rounding (Fig. 7) but the ash generated  
598 preserves the initial textures of the starting material (high vesicularity) resulting in extremely irregular  
599 ash shapes (Fig. 9).

600 Shape and componentry have been linked using BSE images (Liu et al., 2015a); here we extend this to  
601 projected area (Morphologi) images using simple componentry classifications that allowed us to relate  
602 CVX and SLD shape parameters to ash componentry in the 3 $\phi$  grainsize (Fig. 8). We can also use the  
603 shape data to infer componentry from CVX-SLD plots (Fig. S2). From these data, it appears that the  
604 vesicular clast content of the 4 $\phi$  Avellino ash is higher than for the 3 $\phi$  grainsize. This is contrary to  
605 expectation, as the proportion of vesicular fragments typically decreases with grain size when the  
606 bubble diameter approaches the average particle diameter. It is possible that this effect is not apparent

607 between 3 and 4 $\phi$  due to the small modal vesicle size in the Avellino pumice and/or there may be fewer  
608 free crystal grains in the 4 $\phi$  size fraction. This comparison, and our interpretation of the results,  
609 demonstrates the dependency of componentry on grain size and builds on the conclusions of Liu et al.  
610 (2015b) that multiple grain sizes should be characterised for shape and componentry where feasible.  
611 Furthermore, the differences between results from the two methods of shape analysis - BSE and  
612 Morphologi - demonstrate that caution is required when comparing datasets collected by different  
613 methods and protocols (e.g. Liu et al., 2015a).

#### 614 **5.5 Comparison between experimental results and natural settings**

615 The shapes of ash particles produced by experimental and natural processes are not identical. Ash from  
616 a Fuego pyroclastic surge deposit, for example, has higher values of solidity and convexity than the  
617 experimentally generated ash (Fig. 11). This is likely explained by the short duration of our experiments,  
618 the experimental conditions of room (rather than high) temperature and the uniformity (in size and  
619 density) of the starting material. Interestingly, although the experimental ash does not exactly replicate  
620 the natural PDC-surge ash properties (Fig. 11b), the morphologies of the two ash samples are more  
621 similar to each other than to ash produced by primary fragmentation (fall ash from Fuego 2016), which  
622 records a much larger range of CVX and SLD values (Fig. 11a). This suggests that the abrasion  
623 experiments have successfully produced ash with shapes that replicate the shape characteristics of  
624 naturally abraded ash.

625 Ash from the PDC matrix of the Avellino EU3pf deposit also has higher values of SLD and CVX than  
626 the experimental products (Fig. 11c), consistent with more extensive milling in a PDC compared to the  
627 short experimental milling times. An additional difference between the natural and experimental  
628 Avellino ash samples is the large lithic component of the natural PDC-matrix ash (Fig. 11f). These  
629 fragments of lavas, skarn and wall rocks provide evidence for the presence and abrasion of resistant  
630 lithologies during PDC emplacement.

631 The most compelling similarities between the natural and experimental samples, are the Adherence  
632 Factor trends (Fig. 12), which closely match each other for both Fuego and Avellino. Moreover, the

633 AF trend of the intermediate Soufriere Hills pumice (intermediate in both vesicularity and crystallinity)  
634 demonstrates that AF can be used to distinguish abrasion products that have formed from starting  
635 materials with different physical properties, as the efficiency of matrix stripping is dependent on the  
636 vesicularity and microlite content of the matrix. Finally, experiments on Avellino pumice show that  
637 extensive abrasion within a PDC can produce abundant fine ash (mean size  $\sim 30\text{-}60\mu\text{m}$ ). In natural  
638 mixed fallout deposits (deposits containing both fall and material generated in the PDC), the GSDs can  
639 be either uni- or bimodal depending on factors such as the distance from source and the positions relative  
640 to the primary dispersion axis (Engwell and Eychenne, 2016). With increasing distance from the vent,  
641 the GSD becomes unimodal converging on the fine mode as the size of the primary fall ash approaches  
642 the grain size of the ash generated by secondary processes, such as abrasion in PDCs. The fine mode  
643 of the GSDs produced by the abrasion experiments are  $5\phi$  for the Avellino and  $4\phi$  for the Fuego. This  
644 size range not only overlaps with natural co-PDC ash (mean of the fine subpopulations of bimodal  
645 samples), but may also explain the variations in co-PDC ash size from different source volcanoes. For  
646 example co-PDC (blast) ash from Mount St Helens has a mean size of  $5\text{-}6\phi$ , which contrasts with the  
647  $4\phi$  mean of the highly crystalline Fuego samples (Engwell and Eychenne, 2016).

648 The amount and size distribution of fine ash will be a key factor in the development of a co-PDC plume,  
649 which can transport ash to the atmosphere (Woods and Wohletz, 1991). Numerous co-PDC layers  
650 associated with large pumice-rich PDCs are found in the stratigraphic record, including eruptions from  
651 Somma Vesuvius and the nearby Phlegrean fields (e.g., Engwell et al., 2014; Sulpizio et al., 2008).  
652 These deposits support our finding that crystal-poor pumice clasts, such as those that comprise the  
653 Avellino deposit, are susceptible to extensive secondary fragmentation and co-PDC plume formation,  
654 which can greatly enhance ultra-distal transport of fine ash.

655 In contrast, discrete co-PDC ash layers from block and ash flows, such as from Fuego, are much less  
656 common. Evidence of ash generation in such flows comes mainly from observation of the bimodality  
657 of the fallout deposit grainsize (e.g., Engwell and Eychenne, 2016; Eychenne et al., 2012). Nonetheless,  
658 abrasion within block and ash flows can generate sufficient fine ash to increase their mobility, thus  
659 elevating their risk factor (Cole et al., 1998; Fujii and Nakada, 1999). However, we suggest that the

660 elevated groundmass crystallinity of constituent clasts will ultimately limit the smallest grain size that  
661 can be produced by abrasion, and the efficiency of ash generation. Therefore, crystal-rich material in  
662 block and ash flows produced by microlite-rich magma is less likely to produce a co-PDC plume with  
663 a large dispersal extent than low density, low crystallinity pumice flows.

## 664 **6. Conclusions**

665 Previous abrasion experiments have found that low density (high vesicularity) pyroclasts generate more  
666 ash than high density (low vesicularity) pyroclasts. Although generally true in our experiments, we  
667 found that the pyroclast density (vesicularity) alone is insufficient to predict how pyroclastic material  
668 will react to abrasion. The ash-generating potential of pyroclastic material is also controlled by the  
669 crystal content, as well as heterogeneities in bubble and crystal textures. Two key relationships were  
670 observed between the amount of ash generated and the crystal content. Firstly, experiments on  
671 microlite-rich pyroclasts from Fuego volcano showed that increasing the heterogeneity of the crystal  
672 population of a (relatively) low-density clast renders it more resistant to abrasion than a high-density  
673 clast with more uniform phenocryst and groundmass characteristics. Secondly, details of both the  
674 vesicle and crystal content of pyroclasts can encourage clasts to split rather than abrade. Increasing the  
675 frequency of clast splitting enhances the ash-generating potential because splitting creates new irregular  
676 surfaces that are susceptible to abrasion.

677 The vesicularity and crystal content of the starting material strongly influences the properties of the ash  
678 generated by abrasion, in addition to the amount of ash generated. Critically, high microlite crystallinity  
679 limits the generation of very fine ash, as shown by the lower abundance and larger size of the ash  
680 generated in the crystal-rich Fuego experiments (4 $\phi$ ) compared to the crystal-poor Avellino experiments  
681 (5 $\phi$ ). The vesicularity and crystal content of pyroclasts also controls the componentry of ash generated  
682 by abrasion, which in turn influences ash shape and, by extension, elutriation and transport (settling)  
683 properties. Co-PDC ash with mixed componentry, (e.g. mainly free crystals and highly vesicular ash),  
684 poses a challenge to dispersion modelling as typically a single density measurement is required for  
685 dispersion models (e.g., Mastin et al., 2010; Witham et al., 2007). Moreover, the vesicular glass  
686 particles will be preferentially elutriated compared to crystals of the same size, due to their low density,

687 altering the componentry of the ash that is dispersed from the PDC to the atmosphere as evidenced by  
688 crystal-enriched ignimbrite deposits (Sparks and Walker, 1977).

689 Abrasion can also alter ash shape. Ash produced in a PDC-surge deposit from Fuego preserves grains  
690 with reduced roughness compared to natural fall Fuego ash (e.g., Liu et al., 2015a). However, we did  
691 not detect reduced roughness of ash generated by abrasion of the highly vesicular Avellino ash. The  
692 Adherence Factor, which quantifies the amount of matrix adhered to (micro)phenocrysts, is most  
693 effective for distinguishing ash that has undergone different degrees of abrasion (Jones et al., 2016) We  
694 also have shown that AF can clearly distinguish ash from different starting materials due to the  
695 maximum amount of matrix that can be attached to a crystal which is determined by the vesicularity of  
696 the matrix. Efficient abrasion strips the matrix from ash grains and this process is more efficient in high  
697 vesicularity materials with low-crystallinity vesicular groundmass such as the Avellino pumice.

698 When compared to natural samples, the experimentally generated ash differed somewhat from the  
699 natural PDC-surge and PDC-matrix ash samples due to differences in abrasion conditions and the  
700 presence of xenoliths. However, the fine modes of the grainsize distributions produced by the milling  
701 are similar to the fine modal grainsizes measured in natural fallout deposits where co-PDC ash has been  
702 recorded (Engwell and Eychenne, 2016). This suggests the experimental abrasion is effectively  
703 replicating the natural process.

#### 704 **Acknowledgements**

705 This work was completed with support from the AXA Research Fund. We thank B. Voarino and J.  
706 Hanson for their sampling of the Pomici de Avellino deposit and E. Liu for sampling the surge and fall  
707 Fuego ash. We also thank S. Kearns, B. Buse and K. McNamara for their support during SEM and  
708 image analysis. Further thanks extend to L. Gurioli and the volcanology group at Laboratoire Magmas  
709 et Volcans for their help with the Morphologi OPA measurements. Finally we thank J. Gardner for the  
710 editorial handling of the manuscript, and R. Cioni and U. Kueppers for constructive reviews that greatly  
711 improved the quality of this manuscript.

712

713 **Figures, captions and tables (for high quality figures please see separately uploaded pdfs):**

714 Figure 1: Density histograms of the  $-3\phi$  juvenile populations of both Fuego (a) and Avellino (b). The  
715 bins are 0.1gcm<sup>-3</sup> intervals and the number of clasts measured is denoted by 'n'. The diamond, circle  
716 and triangle symbols indicate the mean density of the low density (LD), average density (AD) and high  
717 density (HD) sub-samples, respectively. a.) FUE2a: filled black symbols, FUE3a: white symbols and  
718 FUE5a: open black symbols. b.) Av31a: filled black symbols, Av32a: white symbols and Av33a: open  
719 black symbols. The upper x-axis is the vesicularity (%) calculated using the DRE densities (Houghton  
720 and Wilson, 1989). See Table 1 for the list of samples and experiments.

721 Figure 2: Summary of abrasion experiment apparatus. The Retsch Planetary Ball Mill PM100 consists  
722 of a rotating basal plate and agate-lined 7.5cm diameter milling jar which contains the sample. The  
723 rotation rate and milling duration are input by the user. The sample is retrieved after milling using a  
724 clean fine brush and stored in a tightly sealed sample bag. Between all samples and sub-samples, the  
725 milling jar is cleaned with clean silicon sand, milled for 4 minutes.

726 Figure 3: Textural differences in vesicle populations between Fuego sub-samples from BSE-SEM  
727 images. a.) Low density clast, b.) low density clast with large glomercrysts and increased microlite  
728 content, c.) average density clast and d.) high density clast. The boxes below contain the density of  
729 individual clasts and the results of the two methods of quantifying vesicularity. The VF values are  
730 lower than the VD values for the LD and HD clasts as the 2D imaging tends to exclude the largest  
731 vesicles. e.) to h.) are the vesicle size distributions of the e.), f.) low Density, g.) average density and  
732 h.) high density clasts. Bin sizes are in phi increments.

733 Figure 4: Irregularities in vesicularity and crystal content within Avellino pumice. a.) An example of a  
734 localised area of dense microlite rich melt. b.) A close-up view of the boundary between the two zones  
735 of crystal and vesicle content. c.) An image of an embedded fragment of thermally recrystallised  
736 limestone with large surrounding vesicle likely due to thermal decomposition of the carbonate minerals.

737 Figure 5: Grain size histograms after 4 minutes of milling. The grey bar represents the starting grain  
738 size. ‘Expected trend’ meaning, low density (high vesicularity) sub-samples generate more ash than  
739 high density (low vesicularity) sub-samples.

740 Figure 6: Total grainsize distributions of all samples following 4 minutes of abrasion in a planetary ball  
741 mill. The starting grainsize is represented by the y-axis ( $-3\phi$ ). a.) TGSDs generated following three  
742 abrasion experiments using Fuego juveniles. Different lines styles correspond to different density sub-  
743 samples. b.) The GSDs generated following the abrasion experiments using the Avellino juveniles. The  
744 colours correspond to the histograms in Figure 5. c.) TSGDs of supplementary Avellino experiments.  
745 \*Av31b used a  $-2\phi$  starting grainsize fraction.

746 Figure 7: Box plots of form factor (FF) measurements for *all* milling experiments of Fuego and Avellino  
747 material. Numbered boxes indicate clast count for all three experiments before ( $-3\phi$ ) and after milling  
748 ( $-3$  and  $-2\phi$ ). Black forms at top are examples of binary images used to measure the FF using ImageJ.  
749 The examples are from the F2a AD and Av33a HD sub-samples. Small black boxes indicate outliers,  
750 which only occur in the Avellino data.

751 Figure 8: Morphologi shape analysis of F3a and Av31a AD  $3\phi$  ash using shape factors solidity and  
752 convexity. a.) Fuego ash analysis. b.) Avellino ash analysis. ‘n’ denotes the grain count. The points  
753 are translucent, so the stronger colour indicates more points. The contours are of the kernel density and  
754 are labelled at with the proportion of points they enclose. c.) and d.) are plots of randomly selected  
755 500 grains from the Fuego (c) and Avellino (d) ash that have been split into different components.

756 Figure 9: Results of ImageJ and BSE image analysis of a.) F3a and b.) Av31a  $3\phi$  AD sample ash at  
757 high image resolution ( $\sim 1560$  pixels/mm). Scatter plots of solidity and convexity shown. The contours  
758 and dashed boxes are where the Morphologi results of the same sample plot (Figure 8). Binary images  
759 of ash grains are shown along axes to demonstrate range in shape parameters.

760 Figure 10: Componentry analysis from BSE images of a.) F3a and b.) Av31a  $3\phi$  (125-180  $\mu\text{m}$ ) ash.  
761 The glass category refers to particles that are almost entirely vesicle-free and microlite-free glass.  
762 Images of each component type can be found in Figure S3.



763 Figure 11: Cross-sectional shape analysis of natural and experimental ash samples. a.) to c.) Kernel  
764 density contours of solidity and convexity of a.) natural fall ash from a paroxysm of Volcan de Fuego  
765 in 2016; b.) natural Fuego PDC-surge ash from 2012 (E. Liu, *personal comm.*); c.) natural PDC-matrix  
766 ash from the EU3pf deposit. The contour intervals correspond to those in Figure 8 and are labelled with  
767 the proportion of data they enclose. The shaded contours at the same intervals represent the Fuego F3a  
768 (red) and Avellino Av31a (blue) SLD and CVX data of experimental ash at reduced resolution (~390  
769 pixels/mm). d.) and e). are cumulative frequency plots of convexity and solidity. The dashed lines  
770 correspond to the natural samples which record a higher proportion of high CVX and SLD values than  
771 the equivalent experimental ash sample. f.) BSE image of the natural Avellino PDC-matrix ash,  
772 highlighting the large lithic component.

773 Figure 12: Adherence factor plot of the Avellino and Fuego milling experiments, the natural PDC-  
774 surge and matrix ash samples and the data from two milling experiments carried out by Jones et al.,  
775 (2016) using Soufriere Hills Volcano (SHV) pumice; the latter were shorter duration experiments but  
776 six agate milling balls used so we assume similar milling efficiencies. Adherence Factor is plotted  
777 cumulatively so that each point indicates the percentage of crystals with that AF value or less. AF  
778 values close to 1 represent a large amount of attached matrix.

79 Table 1 – Abrasion experiments and summary: sample names, experiment conditions and subsequent analysis. The ‘sample characterisation’ column lists the clasts that were  
80 mounted for vesicularity and crystal content assessment. Some of the sample characterisation was before milling (BM clasts) and some was done after milling (AM clasts).  
81 The clast shape analysis column signifies the samples where the larger clasts were photographed, and their shape analysed. All experiments started with -3 $\phi$  clasts solely and  
82 lasted 4 minutes, apart from the two additional Avellino experiments Av31b and Av3AG. Av31b used starting material in the -2 $\phi$  fraction and was milled for 5 minutes.  
83 Av3AG included one agate ball as a proxy for a lithic component. FUE003 are average density juveniles from the Fuego PDC deposit not used in the abrasion experiments.  
84 AV-16-01 is an Avellino fall pumice, also not used in the abrasion experiments (Voarino, 2016).

Sample Name	Sub-Samples	No. of clasts BM	No. of clasts AM (remaining in -3 $\phi$ )	No. of clasts AM (in -3 $\phi$ and -2 $\phi$ )	Milling time (mins)	Rotation Rate (rpm)	Sample Characterisation	FOAMS	Clast Shape	Morphologi Analysis	BSE-SEM	
											and ImageJ Analysis	Adherence Factor
FUE2a	LD	10	8	10	4	450	2 x clasts AM	2 x clast	✓		✓ 3 $\phi$	✓ 3 $\phi$
	AD	10	8	11	4	450			✓		✓ 3 $\phi$	✓ 3 $\phi$
	HD	10	9	12	4	450	1 x clast AM		✓		✓ 3 $\phi$	✓ 3 $\phi$
FUE3a	LD	10	4	9	4	450	1 x clast AM	1 x clast	✓	✓ 3 $\phi$ , 4 $\phi$	✓ 3 $\phi$	
	AD	10	6	12	4	450	2 x clast AM	2 x clast	✓	✓ 3 $\phi$ , 4 $\phi$	✓ 3 $\phi$	
	HD	10	8	10	4	450		1 x clast	✓	✓ 3 $\phi$ , 4 $\phi$	✓ 3 $\phi$	
FUE5a	LD	10	7	11	4	450	1 x clast AM	1 x clast	✓			
	AD	10	5	13	4	450			✓			
	HD	10	4	13	4	450	1 x clast AM	1 x clast	✓			
<b>FUE003</b>							2 x clast BM	1 x clast				
Av31a	LD	7	1	6	4	450	3 x clasts AM		✓	✓ 3 $\phi$ , 4 $\phi$	✓ 3 $\phi$	✓ 3 $\phi$
	AD	7	3	7	4	450	2 x clasts AM		✓	✓ 3 $\phi$ , 4 $\phi$	✓ 3 $\phi$	✓ 3 $\phi$
	HD	7	1	10	4	450	4 x clasts AM		✓	✓ 3 $\phi$ , 4 $\phi$	✓ 3 $\phi$	✓ 3 $\phi$
Av32a	LD	8*	1	12	4	450			✓			
	AD	7	2	10	4	450	1 x clast AM		✓			
	HD	7	3	7	4	450			✓			
Av33a	LD	7	1	7	4	450			✓		✓ 3 $\phi$	
	AD	7	2	7	4	450			✓		✓ 3 $\phi$	
	HD	7	1	9	4	450	1 x clast AM		✓		✓ 3 $\phi$	
Av31b	LD	40		15	5	450						
	AD	40		38	5	450						
	HD	40		42	5	450						
Av3AG	AD	7	5	9	4	450			✓		✓ 3 $\phi$	
	<b>AV-16-01</b>		<i>Avellino fall pumice not used in abrasion experiments, only vesicularity characterisation</i>				2 x clast	1 x clast				

\* There were 7 clasts but one broke during loading prior to milling

\*\* Imaging and FOAMS analysis carried out by Voarino, (2016).

Table 2 – Shape parameters and definitions. This table only highlights key parameters used in this study, see Liu et al., (2015) for a comprehensive summary of shape factors and uses.

Shape Parameter	Abbreviation	Formula	Symbols	Sensitivity	Alternative nomenclature	References
<i>Form Factor</i>	FF	$4\pi A_p / P_p^2$	$A_p$ = area of particle $P_p$ = perimeter of particle	Form and roughness	Sphericity, Roundness, Circularity, HS Circularity, Shape Factor, Cox circularity	Liu et al., 2016 and references within
<i>Solidity</i>	SLD	$A_p / A_{CH}$	$A_p$ = area of particle $A_{CH}$ = area of convex hull	Roughness (morphological)		Liu et al., 2016
<i>Convexity</i>	CVX	$P_{CH} / P_p$	$P_{CH}$ = perimeter of convex hull $P_p$ = perimeter of particle	Roughness (textural)	Roughness	Liu et al., 2016
<i>Adherence Factor</i>	AF	$A_M / A_M + A_C$	$A_M$ = area of attached matrix $A_C$ = area of crystal	Amount of attached matrix	Abrasion index ( $A_p / A_M$ )	Jones et al., 2016, Freundt & Schminke, 1992

## References

- Andronico, D., Cioni, R., 2002. Contrasting styles of Mount Vesuvius activity in the period between the Avellino and Pompeii Plinian eruptions, and some implications for assessment of future hazards. *Bull. Volcanol.* 64, 372–391. doi:10.1007/s00445-002-0215-4
- Balcone-Boissard, H., Boudon, G., Ucciani, G., Villemant, B., Cioni, R., Civetta, L., Orsi, G., 2012. Magma degassing and eruption dynamics of the Avellino pumice Plinian eruption of Somma-Vesuvius (Italy). Comparison with the Pompeii eruption. *Earth Planet. Sci. Lett.* 331–332, 257–268. doi:10.1016/j.epsl.2012.03.011
- Berlo, K., Stix, J., Roggensack, K., Ghaleb, B., 2012. A tale of two magmas, Fuego, Guatemala. *Bull. Volcanol.* 74, 377–390. doi:10.1007/s00445-011-0530-8
- Bernard, J., Le Pennec, J.L., 2016. The milling factory: Componentry-dependent fragmentation and fines production in pyroclastic flows. *Geology* 44, 907–910. doi:10.1130/G38198.1
- Bindeman, I.N., 2005. Fragmentation phenomena in populations of magmatic crystals. *Am. Mineral.* 90, 1801–1815. doi:10.2138/am.2005.1645
- Chesner, C.A., Rose, W.I., 1984. Geochemistry and evolution of the Fuego volcanic complex, Guatemala. *J. Volcanol. Geotherm. Res.* 21, 25–44. doi:10.1016/0377-0273(84)90014-3
- Chigna, G., Giron, J., Barrios, E., Calderas, A., Cornejo, J., 2012. Reporte de la erupcion del volcan fuego 13 septiembre 2012.
- Cioni, R., Santacroce, R., Sbrana, A., 1999. Pyroclastic deposits as a guide for reconstructing the multi-stage evolution of the Somma-Vesuvius Caldera. *Bull. Volcanol.* 61, 207–222.
- Cole, P.D., Calder, E.S., Druitt, T.H., Hoblitt, R., Robertson, R., Sparks, R.S.J., 1998. Pyroclastic flows generated by gravitational instability of the 1996-97 lava dome of Soufriere Hills Volcano, Montserrat. *Geophys. Res. Lett.* 25, 3425–3428.
- Cole, P.D., Calder, E.S., Sparks, R.S.J., Clarke, A.B., Druitt, T.H., Young, S.R., Herd, R.A., Harford,

- C.L., Norton, G.E., 2002. Deposits from dome-collapse and fountain-collapse pyroclastic flows at Soufrière Hills Volcano, Montserrat. *Geol. Soc. London, Mem.* 21, 231 LP-262.
- Coltelli, M., Miraglia, L., Scollo, S., 2008. Characterization of shape and terminal velocity of tephra particles erupted during the 2002 eruption of Etna volcano, Italy. *Bull. Volcanol.* 70, 1103–1112. doi:10.1007/s00445-007-0192-8
- Dufek, J., Manga, M., 2008. In situ production of ash in pyroclastic flows. *J. Geophys. Res. Earth* 113. doi:10.1029/2007jb005555
- Dufek, J., Manga, M., Patel, A., 2012. Granular disruption during explosive volcanic eruptions. *Nat. Geosci.* 5, 561–564. doi:10.1038/ngeo1524
- Durant, A.J., Rose, W.I., 2009. Sedimentological constraints on hydrometeor-enhanced particle deposition: 1992 Eruptions of Crater Peak, Alaska. *J. Volcanol. Geotherm. Res.* 186, 40–59. doi:10.1016/j.jvolgeores.2009.02.004
- Engwell, S., Eychenne, J., 2016. Chapter 4 – Contribution of Fine Ash to the Atmosphere From Plumes Associated With Pyroclastic Density Currents, in: *Volcanic Ash*. pp. 67–85. doi:10.1016/B978-0-08-100405-0.00007-0
- Engwell, S.L., Sparks, R.S.J., Carey, S., 2014. Physical characteristics of tephra layers in the deep sea realm: the Campanian Ignimbrite eruption. *Mar. Tephrochronology* 398, 47–64. doi:10.1144/SP398.7
- Engwell, S.L., Vitturi, M.D., Ongaro, T.E., Neri, A., 2016. Insights into the formation and dynamics of coignimbrite plumes from one-dimensional models. *J. Geophys. Res. Earth* 121, 4211–4231. doi:10.1002/2016jb012793
- Eychenne, J., Le Pennec, J.L., Troncoso, L., Gouhier, M., Nedelec, J.M., 2012. Causes and consequences of bimodal grain-size distribution of tephra fall deposited during the August 2006 Tungurahua eruption (Ecuador). *Bull. Volcanol.* 74, 187–205. doi:10.1007/s00445-011-0517-5
- Ferreira, T., Rasband, W., 2012. ImageJ User Guide IJ 1.46r. IJ 1.46r 185. doi:10.1038/nmeth.2019

- Freundt, A., Schmincke, H.U., 1992. Abrasion in pyroclastic flows. *Geol. Rundschau* 81, 383–389.  
doi:10.1007/bf01828605
- Fujii, T., Nakada, S., 1999. The 15 September 1991 pyroclastic flows at Unzen Volcano (Japan): a flow model for associated ash-cloud surges. *J. Volcanol. Geotherm. Res.* 89, 159–172.  
doi:10.1016/S0377-0273(98)00130-9
- Gardner, C.A., Cashman, K. V., Neal, C.A., 1998. Tephra-fall deposits from the 1992 eruption of Crater Peak, Alaska: implications of clast textures for eruptive processes. *Bull. Volcanol.* 59, 537–555. doi:10.1007/s004450050208
- Gonnermann, H.M., 2015. Magma Fragmentation. *Annu. Rev. Earth Planet. Sci.* Vol 43 43, 431–458.  
doi:10.1146/annurev-earth-060614-105206
- Gravina, T., Lirer, L., Marzocchella, A., Petrosino, P., Salatino, P., 2004. Fluidization and attrition of pyroclastic granular solids. *J. Volcanol. Geotherm. Res.* 138, 27–42.  
doi:10.1016/j.jvolgeores.2004.06.005
- Gudmundsson, M.T., Thordarson, T., Hoskuldsson, A., Larsen, G., Bjornsson, H., Prata, F.J., Oddsson, B., Magnusson, E., Hognadottir, T., Petersen, G.N., Hayward, C.L., Stevenson, J.A., Jonsdottir, I., 2012. Ash generation and distribution from the April-May 2010 eruption of Eyjafjallajokull, Iceland. *Sci. Rep.* 2. doi:10.1038/srep00572
- Heap, M.J., Wadsworth, F.B., Xu, T., Chen, C. feng, Tang, C., 2016. The strength of heterogeneous volcanic rocks: A 2D approximation. *J. Volcanol. Geotherm. Res.* 319, 1–11.  
doi:10.1016/j.jvolgeores.2016.03.013
- Heap, M.J., Xu, T., Chen, C., 2014. The influence of porosity and vesicle size on the brittle strength of volcanic rocks and magma. *Bull. Volcanol.* 76, 1–15.
- Horwell, C.J., 2007. Grain-size analysis of volcanic ash for the rapid assessment of respiratory health hazard. *J. Environ. Monit.* 9, 1107–1115. doi:10.1039/010583p
- Houghton, B.F., Wilson, C.J.N., 1989. A vesicularity index for pyroclastic rocks. *Bull. Volcanol.* 51,

451–462. doi:10.1007/bf01078811

Jolis, E.M., Troll, V.R., Harris, C., Freda, C., Gaeta, M., Orsi, G., Siebe, C., 2015. Skarn xenolith record crustal CO<sub>2</sub> liberation during Pompeii and Pollena eruptions, Vesuvius volcanic system, central Italy. *Chem. Geol.* 415, 17–36. doi:10.1016/j.chemgeo.2015.09.003

Jones, T.J., McNamara, K., Eychenne, J., Rust, A.C., Cashman, K. V, Scheu, B., Edwards, R., 2016. Primary and secondary fragmentation of crystal bearing intermediate magma. *J. Volcanol. Geotherm. Res.* doi:10.1016/j.jvolgeores.2016.06.022

Kueppers, U., Putz, C., Spieler, O., Dingwell, D.B., 2012. Abrasion in pyroclastic density currents: Insights from tumbling experiments. *Phys. Chem. Earth* 45–46, 33–39. doi:10.1016/j.pce.2011.09.002

Leibrandt, S., Le Pennec, J.L., 2015. Towards fast and routine analyses of volcanic ash morphometry for eruption surveillance applications. *J. Volcanol. Geotherm. Res.* 297, 11–27. doi:10.1016/j.jvolgeores.2015.03.014

Liu, E.J., Cashman, K. V, Rust, A.C., 2015a. Optimising shape analysis to quantify volcanic ash morphology. *GeoResJ* 8, 14–30. doi:http://dx.doi.org/10.1016/j.grj.2015.09.001

Liu, E.J., Cashman, K. V, Rust, A.C., Gislason, S.R., 2015b. The role of bubbles in generating fine ash during hydromagmatic eruptions. *Geology* 43, 239–242. doi:10.1130/g36336.1

Lu, S.-Y., Mao, Q.-J., Peng, Z., Li, X.-D., Yan, J.-H., 2012. Simulation of ball motion and energy transfer in a planetary ball mill. *Chinese Phys. B* 21, 78201. doi:10.1088/1674-1056/21/7/078201

Manga, M., Patel, A., Dufek, J., 2011. Rounding of pumice clasts during transport: field measurements and laboratory studies. *Bull. Volcanol.* 73, 321–333. doi:10.1007/s00445-010-0411-6

Maria, A., Carey, S., 2007. Quantitative discrimination of magma fragmentation and pyroclastic transport processes using the fractal spectrum technique. *J. Volcanol. Geotherm. Res.* 161, 234–

246. doi:10.1016/j.jvolgeores.2006.12.006

- Marti, A., Folch, A., Costa, A., Engwell, S., 2016. Reconstructing the plinian and co-ignimbrite sources of large volcanic eruptions: A novel approach for the Campanian Ignimbrite. *Sci. Rep.* 6, 11. doi:10.1038/srep21220
- Mastin, L.G., Guffanti, M., Servranckx, R., Webley, P., Barsotti, S., Dean, K., Durant, A., Ewert, J.W., Neri, A., Rose, W.I., Schneider, D., Siebert, L., Stunder, B., Swanson, G., Tupper, A., Volentik, A., Waythomas, C.F., 2010. A multidisciplinary effort to assign realistic source parameters to models of volcanic ash-cloud transport and dispersion during eruptions (vol 188, pg 1, 2009). *J. Volcanol. Geotherm. Res.* 191, 245. doi:10.1016/j.jvolgeores.2009.10.013
- Mio, H., Kano, J., Saito, F., Kaneko, K., 2002. Effects of rotational direction and rotation-to-revolution speed ratio in planetary ball milling. *Mater. Sci. Eng. A* 332, 75–80. doi:10.1016/S0921-5093(01)01718-X
- Mueller, S.B., Lane, S.J., Kueppers, U., 2015. Lab-scale ash production by abrasion and collision experiments of porous volcanic samples. *J. Volcanol. Geotherm. Res.* 302, 163–172. doi:10.1016/j.jvolgeores.2015.07.013
- Oppenheimer, J., Rust, A.C., Cashman, K. V., Sandnes, B., 2015. Gas migration regimes and outgassing in particle-rich suspensions. *Front. Phys.* 3, 1–13. doi:10.3389/fphy.2015.00060
- Parmigiani, A., Faroughi, S., Huber, C., Bachmann, O., Su, Y., 2016. Bubble accumulation and its role in the evolution of magma reservoirs in the upper crust. *Nature*. doi:10.1038/nature17401
- Parmigiani, A., Huber, C., Bachmann, O., Chopard, B., 2011. Pore-scale mass and reactant transport in multiphase porous media flows. *J. Fluid Mech.* 686, 40–76. doi:10.1017/jfm.2011.268
- Rose, W.I., Durant, A.J., 2009. Fine ash content of explosive eruptions. *J. Volcanol. Geotherm. Res.* 186, 32–39. doi:10.1016/j.jvolgeores.2009.01.010
- Rose, W.I., Self, S., Murrow, P.J., Bonadonna, C., Durant, A.J., Ernst, G.G.J., 2008. Nature and significance of small volume fall deposits at composite volcanoes: Insights from the October 14,

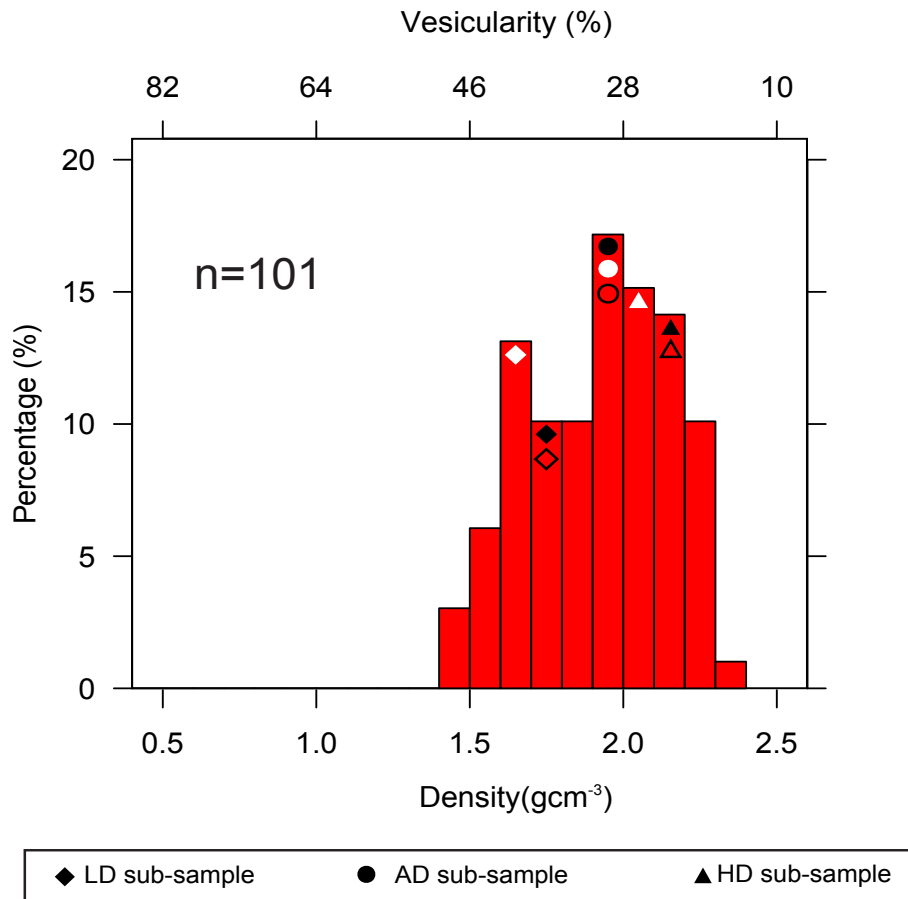


- 1974 Fuego eruption, Guatemala. *Bull. Volcanol.* 70, 1043–1067. doi:10.1007/s00445-007-0187-5
- Rust, A.C., Cashman, K. V, 2011. Permeability controls on expansion and size distributions of pyroclasts. *J. Geophys. Res. Earth* 116. doi:10.1029/2011jb008494
- Shea, T., Hammer, J.E., 2013. Kinetics of cooling- and decompression-induced crystallization in hydrous mafic-intermediate magmas. *J. Volcanol. Geotherm. Res.* 260, 127–145. doi:10.1016/j.jvolgeores.2013.04.018
- Shea, T., Houghton, B.F., Gurioli, L., Cashman, K. V, Hammer, J.E., Hobden, B.J., 2010. Textural studies of vesicles in volcanic rocks: An integrated methodology. *J. Volcanol. Geotherm. Res.* 190, 271–289. doi:10.1016/j.jvolgeores.2009.12.003
- Sottili, G., Taddeucci, J., Palladino, D.M., 2010. Constraints on magma-wall rock thermal interaction during explosive eruptions from textural analysis of cored bombs. *J. Volcanol. Geotherm. Res.* 192, 27–34. doi:10.1016/j.jvolgeores.2010.02.003
- Sparks, R.S.J., Bursik, M.I., Carey, S., Gilbert, J., Glaze, L., Sigurdsson, H., Woods, A.W., 1997. *Volcanic plumes*. Wiley.
- Sparks, R.S.J., Self, S., Walker, G.P.L., 1973. Products of ignimbrite eruptions. *Geology* 1, 115–118. doi:10.1130/0091-7613(1973)1<115:POIE>2.0.CO;2
- Sparks, R.S.J., Walker, G.P.L., 1977. SIGNIFICANCE OF VITRIC-ENRICHED AIR-FALL ASHES ASSOCIATED WITH CRYSTAL-ENRICHED IGNIMBRITES. *J. Volcanol. Geotherm. Res.* 2, 329–341. doi:10.1016/0377-0273(77)90019-1
- Sulpizio, R., Bonasia, R., Dellino, P., Di Vito, M.A., La Volpe, L., Mele, D., Zanchetta, G., Sadori, L., 2008. Discriminating the long distance dispersal of fine ash from sustained columns or near ground ash clouds: The example of the Pomici di Avellino eruption (Somma-Vesuvius, Italy). *J. Volcanol. Geotherm. Res.* 177, 263–276. doi:10.1016/j.jvolgeores.2007.11.012
- Sulpizio, R., Bonasia, R., Dellino, P., Mele, D., Di Vito, M.A., La Volpe, L., 2010a. The Pomici di

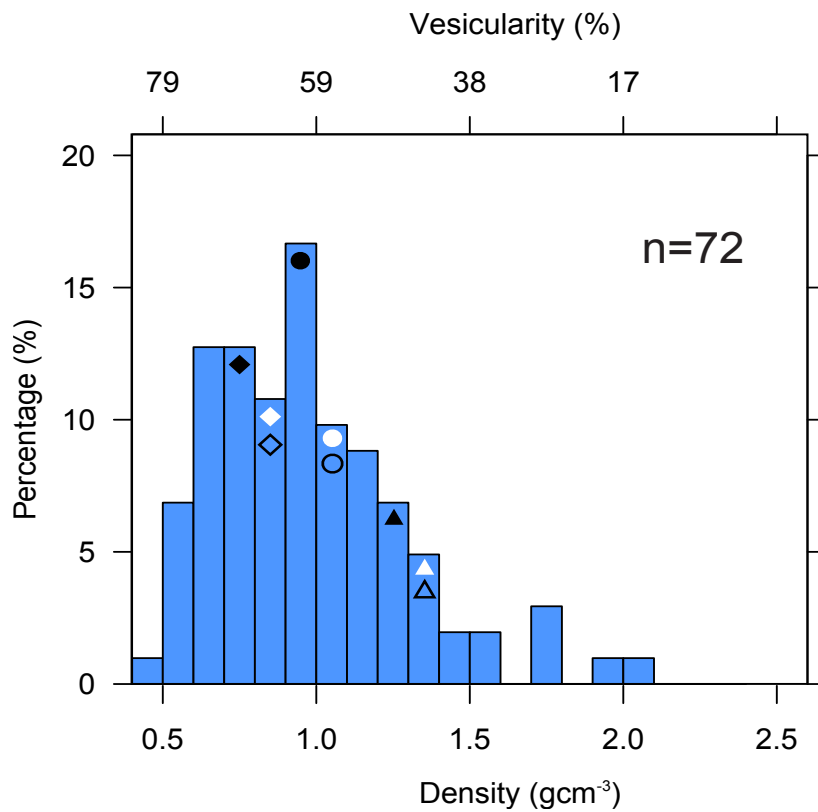
- Avellino eruption of Somma-Vesuvius (3.9 ka BP). Part II: sedimentology and physical volcanology of pyroclastic density current deposits. *Bull. Volcanol.* 72, 559–577.  
doi:10.1007/s00445-009-0340-4
- Sulpizio, R., Cioni, R., Di Vito, M.A., Mele, D., Bonasia, R., Dellino, P., 2010b. The Pomici di Avellino eruption of Somma-Vesuvius (3.9 ka bp). Part I: stratigraphy, compositional variability and eruptive dynamics. *Bull. Volcanol.* 72, 539–558. doi:10.1007/s00445-009-0339-x
- Taddeucci, J., Palladino, D.M., 2002. Particle size-density relationships in pyroclastic deposits: inferences for emplacement processes. *Bull. Volcanol.* 64, 273–284. doi:10.1007/s00445-002-0205-6
- Thomson, B.J., Bridges, N.T., Cohen, J., Hurowitz, J.A., Lennon, A., Paulsen, G., Zacny, K., 2013. Estimating rock compressive strength from Rock Abrasion Tool (RAT) grinds. *J. Geophys. Res. Planets* 118, 1233–1244.
- Turcotte, D.L., 1986. Fractals and fragmentation. *J. Geophys. Res. Earth Planets* 91, 1921–1926.  
doi:10.1029/JB091iB02p01921
- Voarino, B., 2016. Insights into fragmentation and column collapse triggers : A study of juvenile density and vesicle textures from the Pomici di Avellino steady plinian phase Brennus Voarino. MSc Thesis Sept. 2016. University of Bristol.
- Walker, G.P.L., 1981. Generation and dispersal of fine ash and dust by volcanic eruptions. *J. Volcanol. Geotherm. Res.* 11, 81–92. doi:10.1016/0377-0273(81)90077-9
- Wawersik, W.R., Fairhurst, C., 1970. A study of brittle rock fracture in laboratory compression experiments. *Int. J. Rock Mech. Min. Sci.* 7, 561–+. doi:10.1016/0148-9062(70)90007-0
- Witham, C.S., Hort, M.C., Potts, R., Servranckx, R., Husson, P., Bonnardot, F., 2007. Comparison of VAAC atmospheric dispersion models using the 1 November 2004 Grimsvötn eruption. *Meteorol. Appl.* 14, 27–38. doi:10.1002/met.3
- Woods, A.W., Wohletz, K., 1991. Dimensions and dynamics of co-ignimbrite eruption columns.

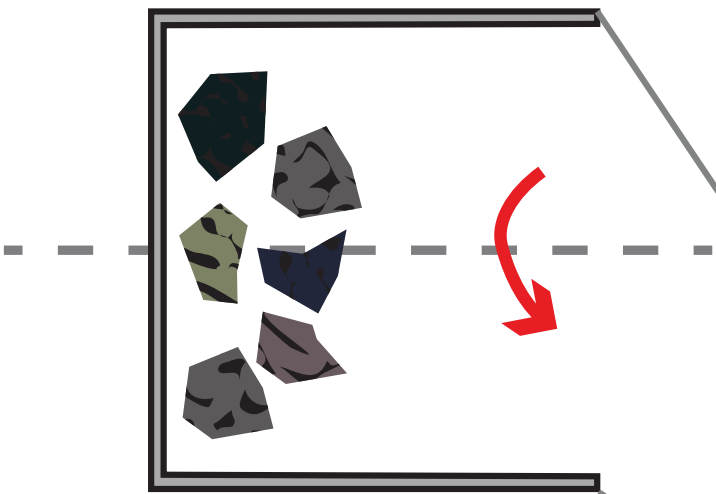
Nature 350, 225–227. doi:10.1038/350225a0

### a.) Fuego



### b.) Avellino

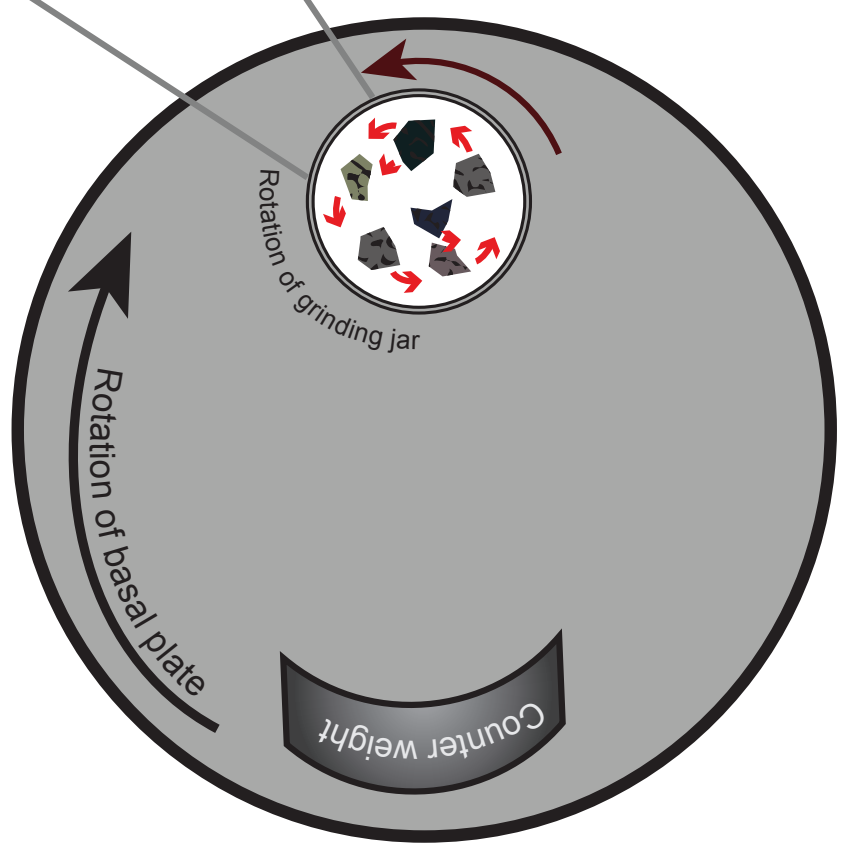




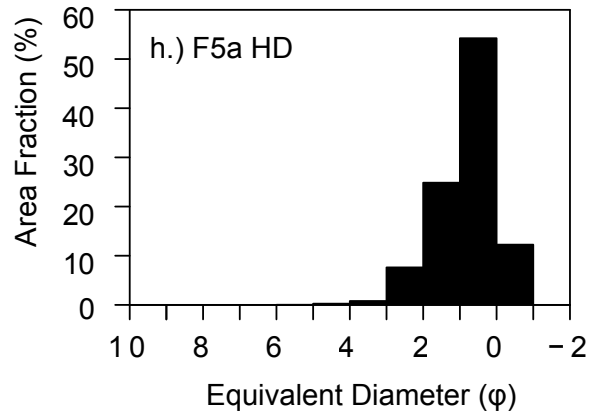
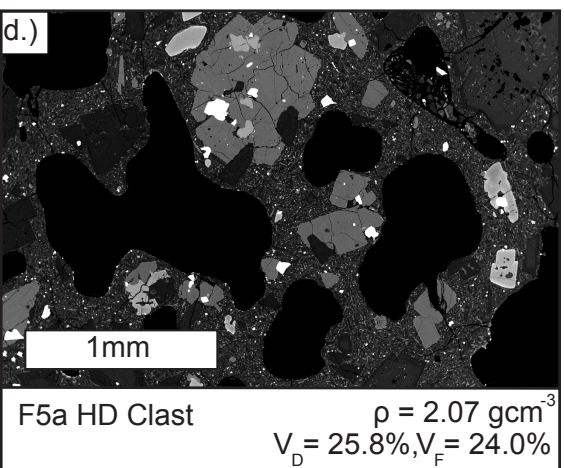
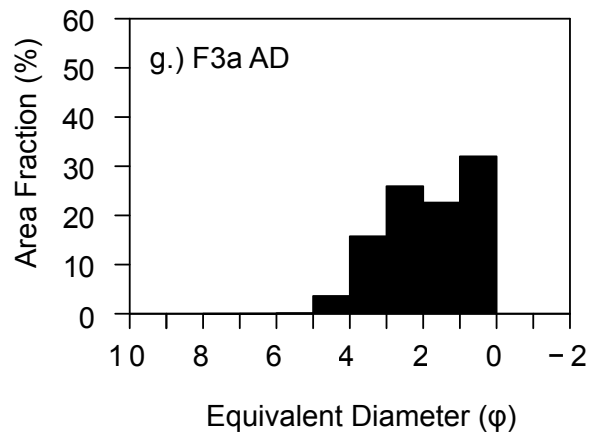
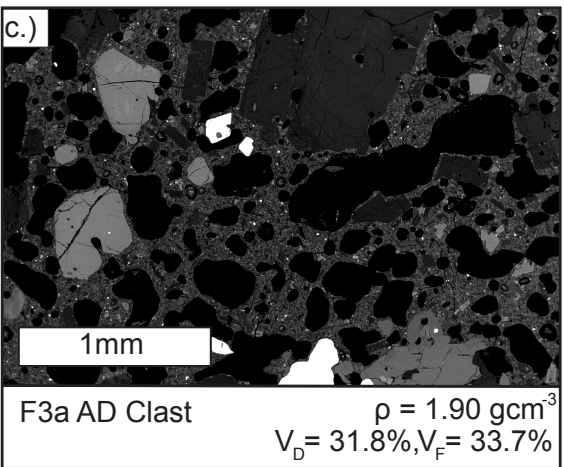
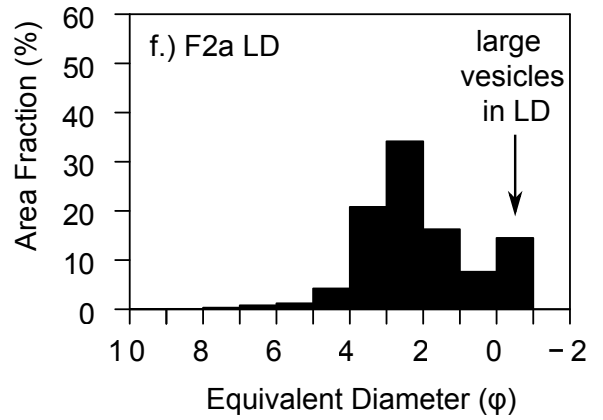
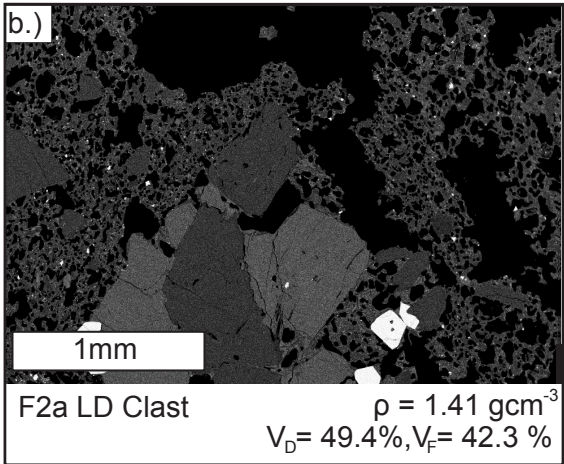
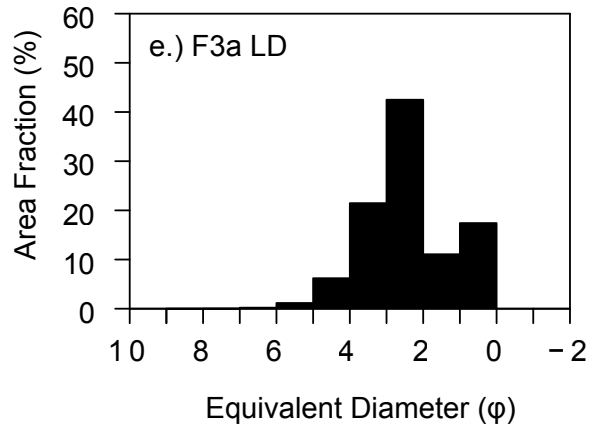
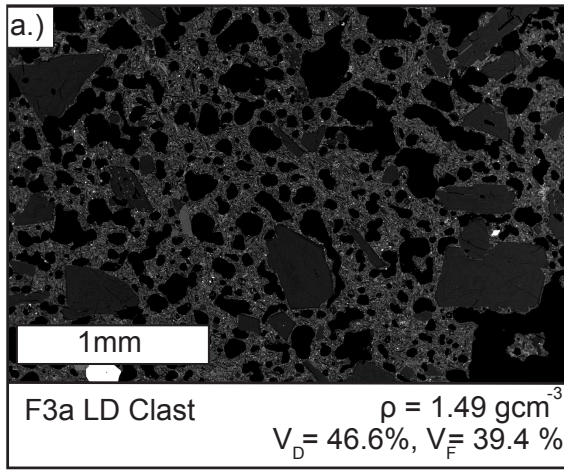
Grinding jar filled with juveniles clasts prior to milling

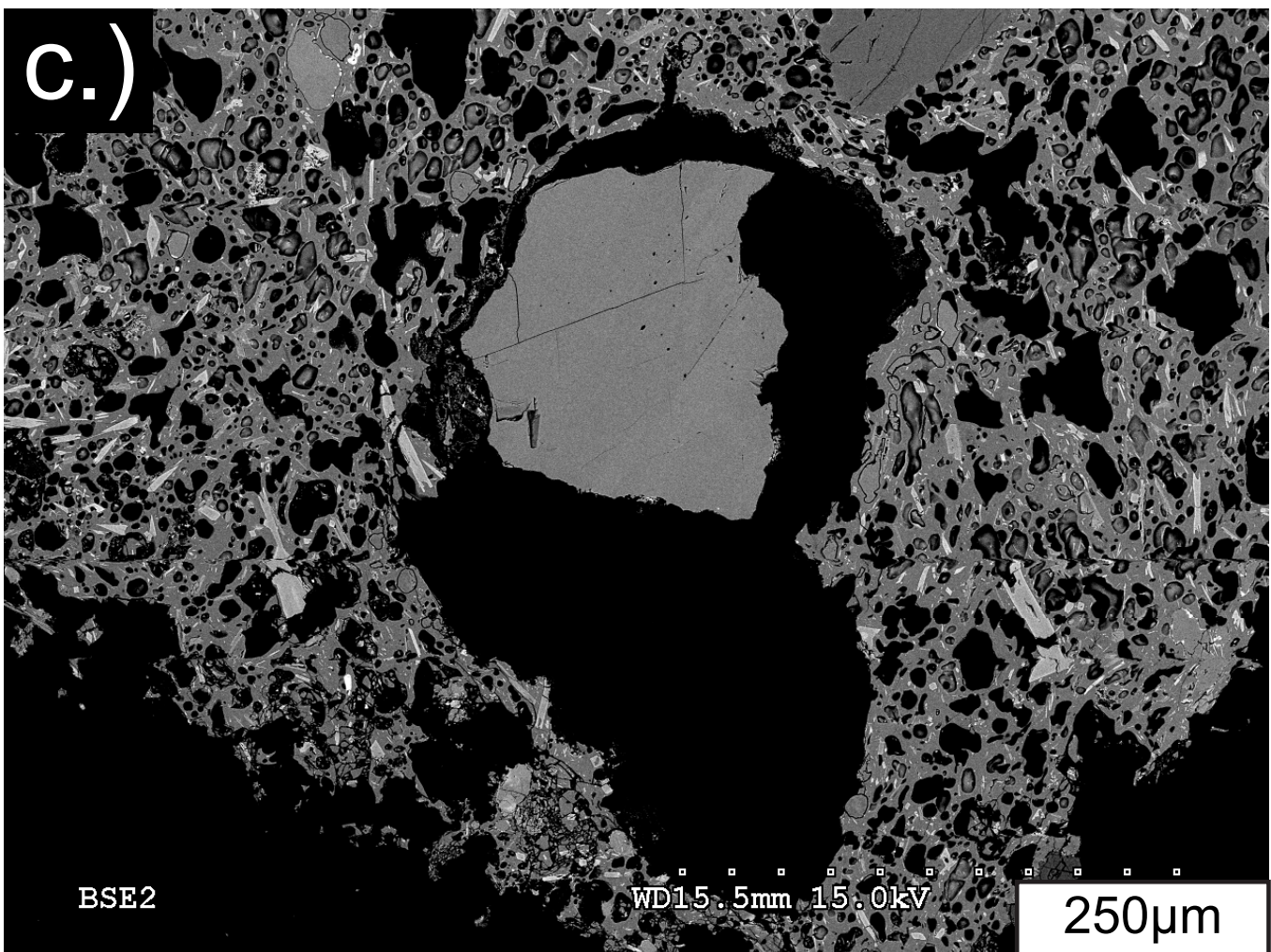
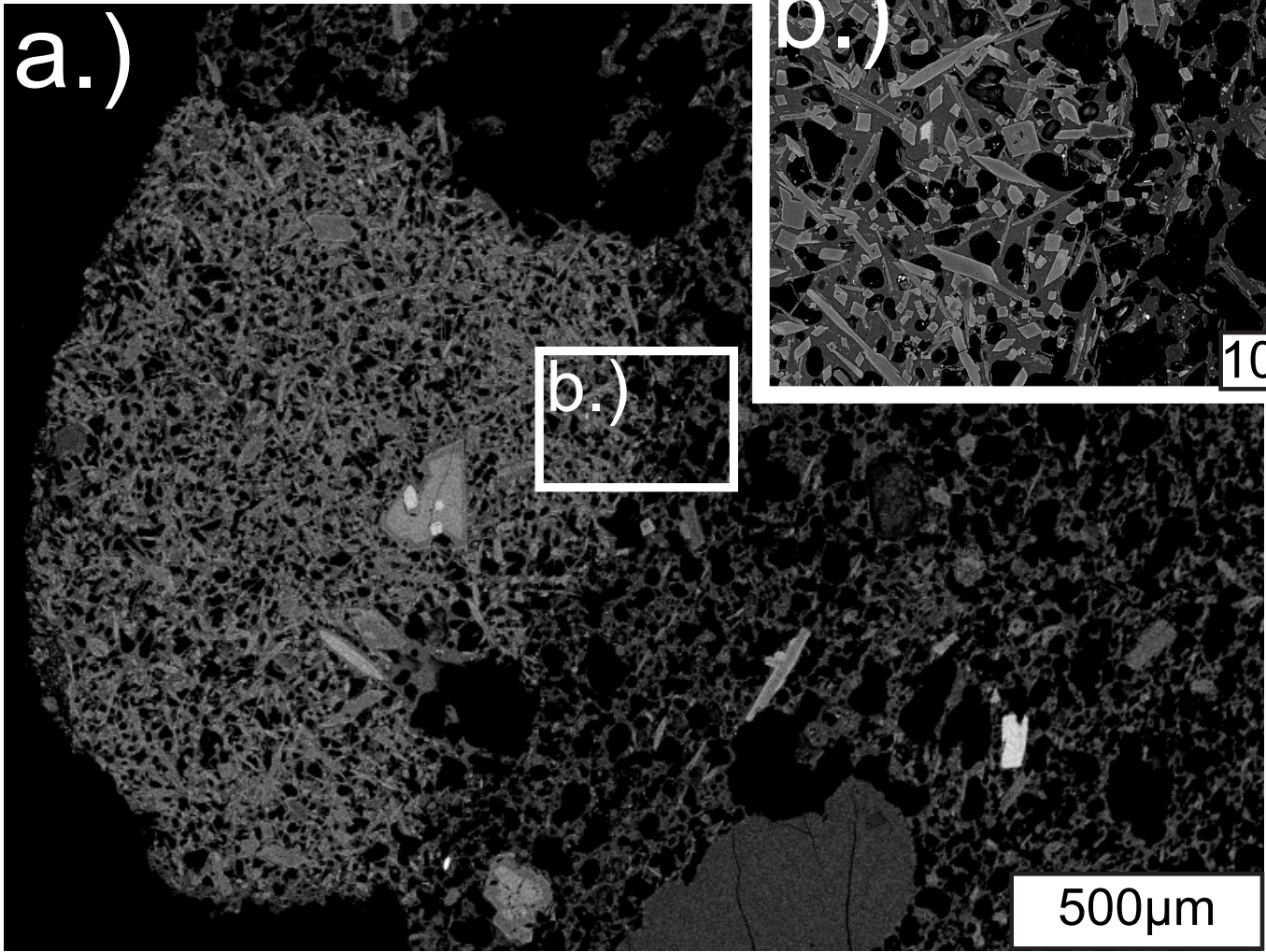


Post abrasion jar filled with clasts and ash to be removed with fine brush



- User sets:
- Rotation rate (rpm)
  - Duration of milling

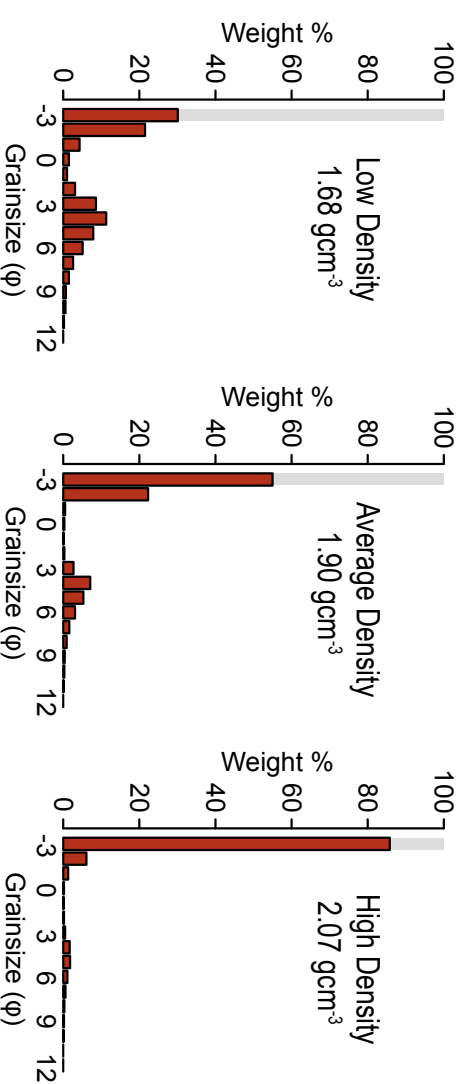




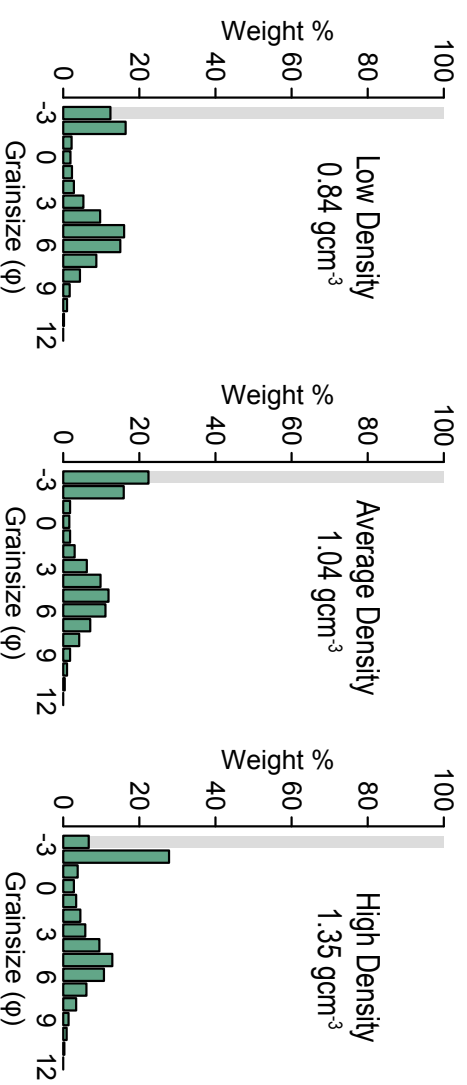
# FUEGO

# AVELLINO

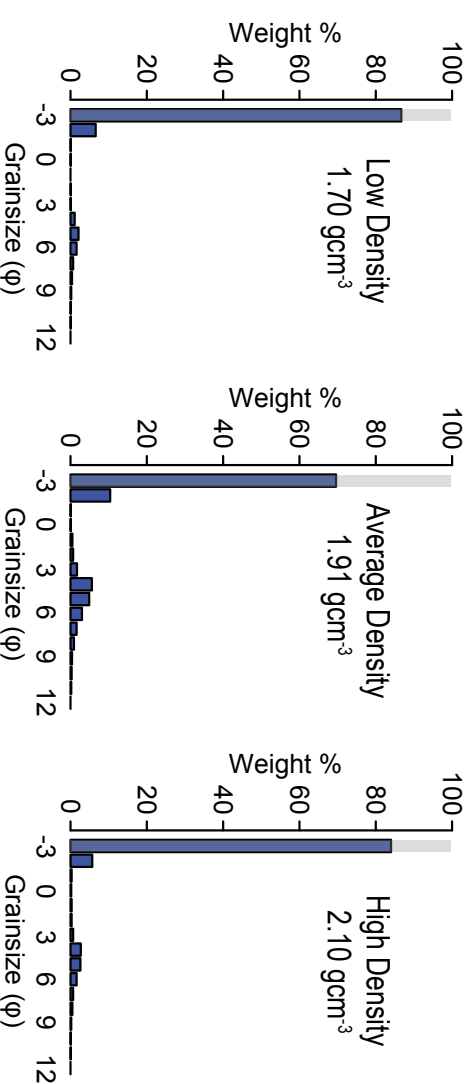
a.) Expected trend (F3a)



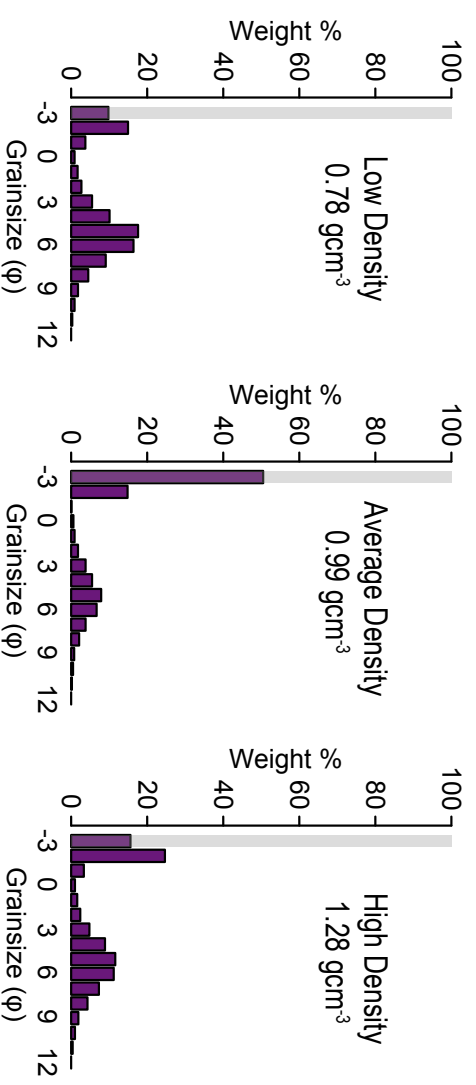
b.) Expected trend (Av33a)



c.) Unexpected trend (F2a)

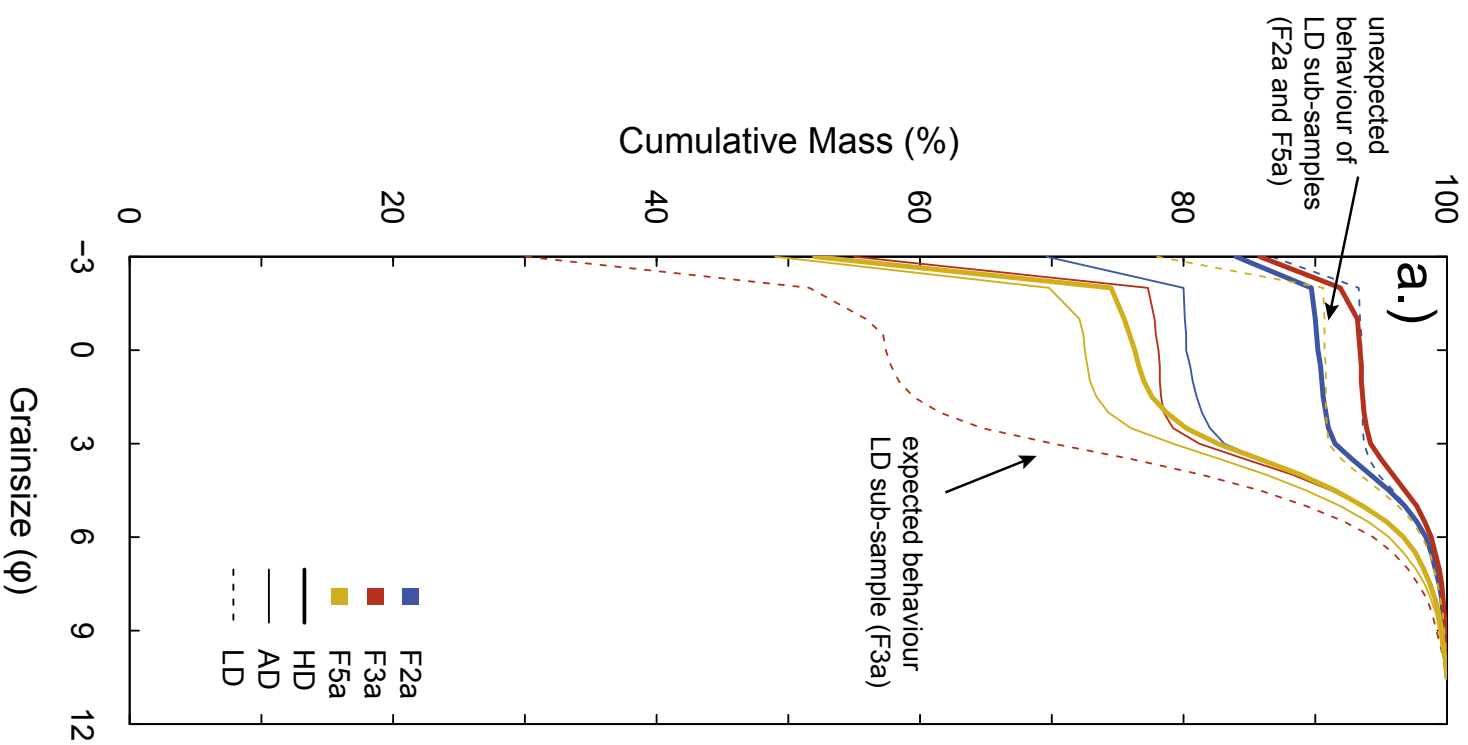


d.) Unexpected trend (Av31a)

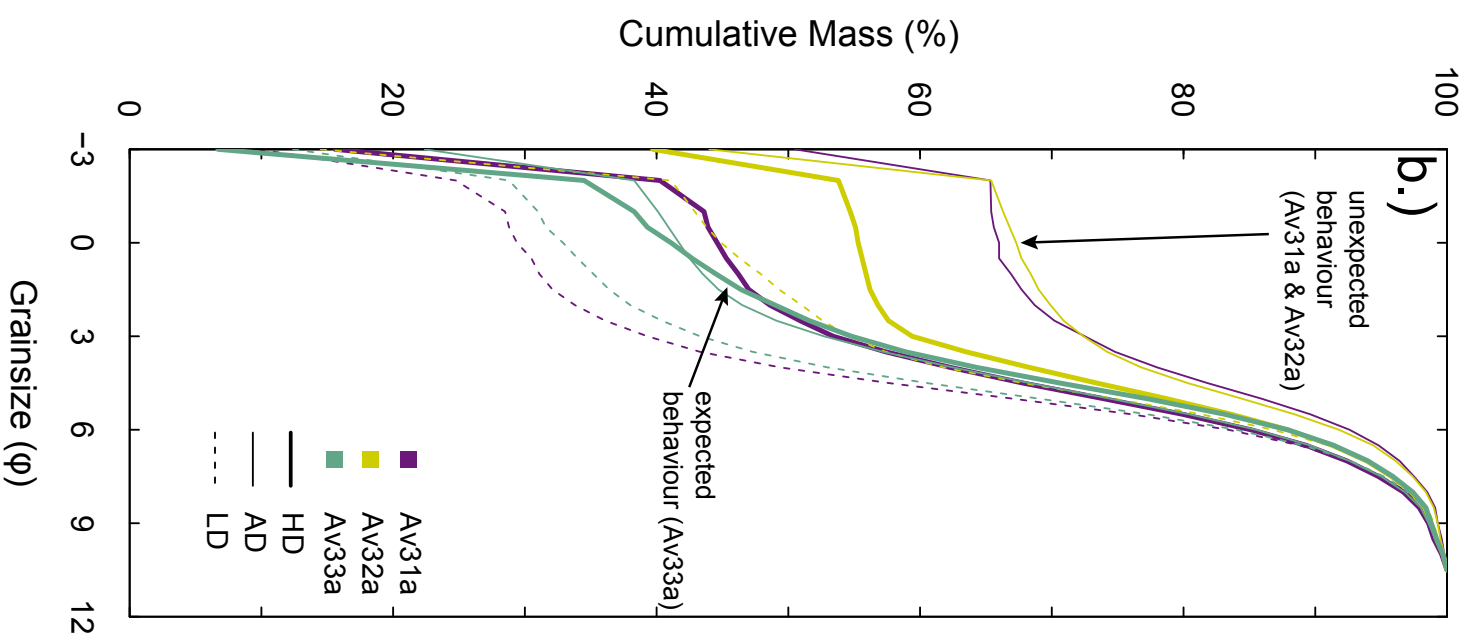




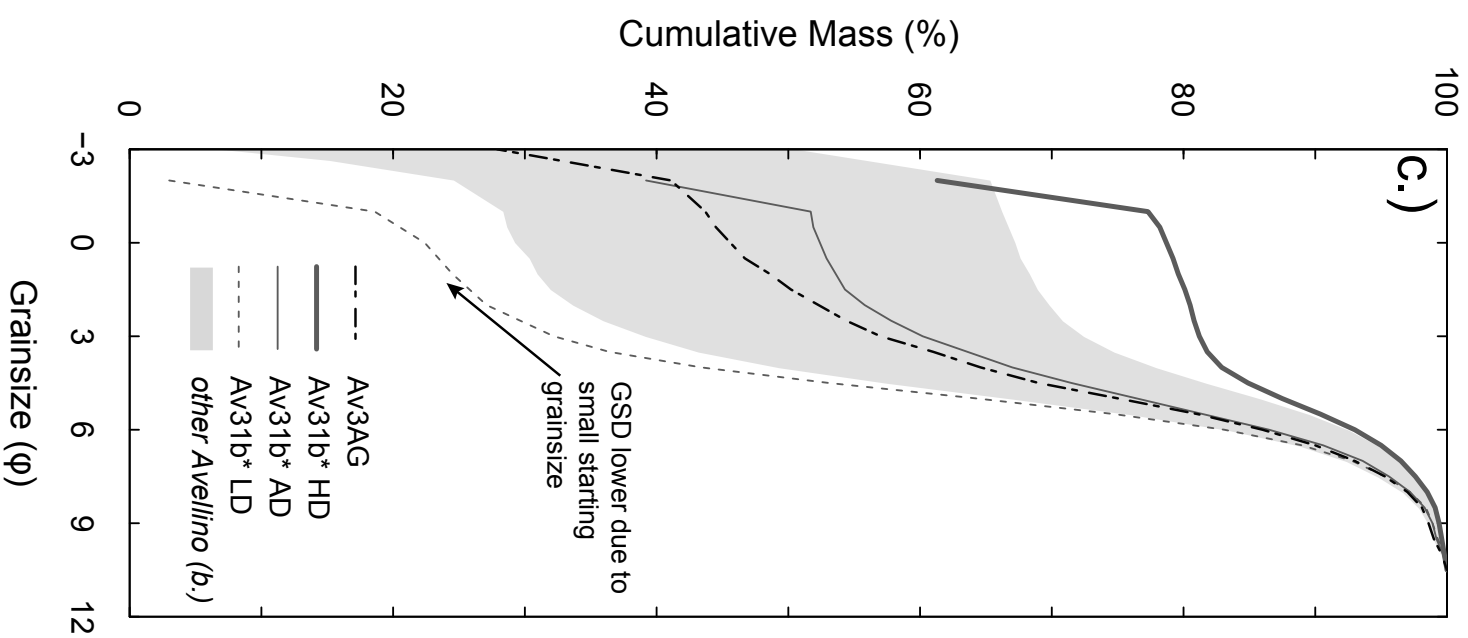
### FUEGO



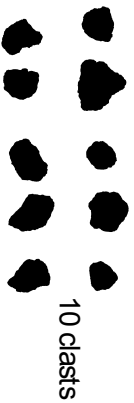
### AVELLINO



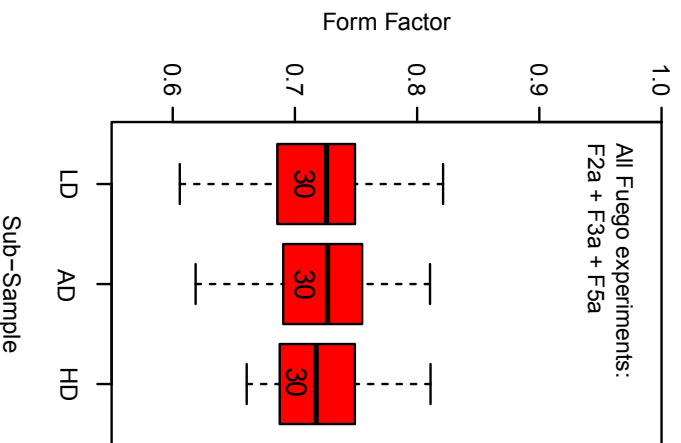
### AVELLINO



### Fuego Before



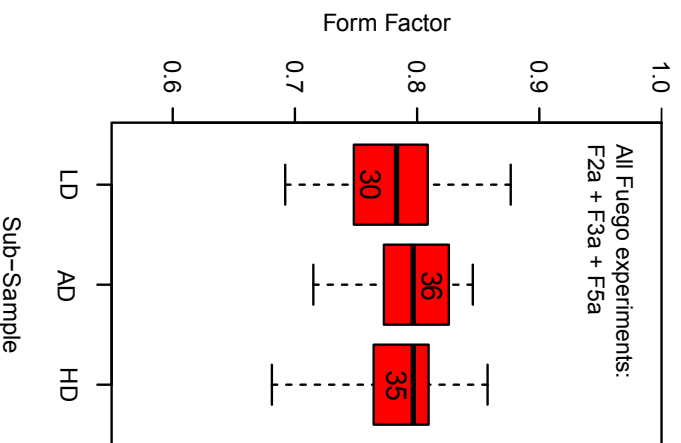
20mm  
e.g. F2a AD



### Fuego After

11 clasts

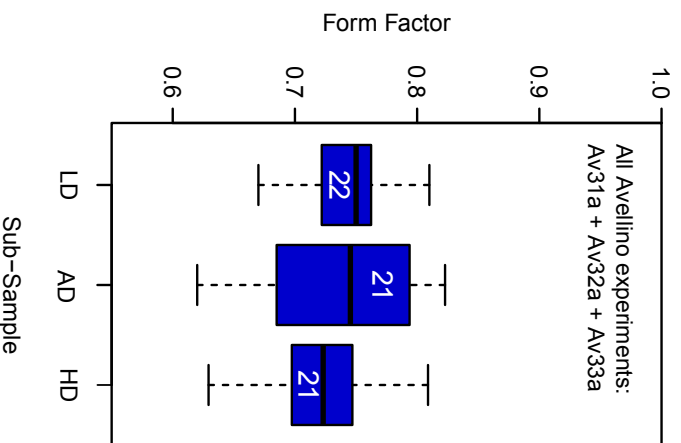
20mm  
e.g. F2a AD



### Avellino Before

7 clasts

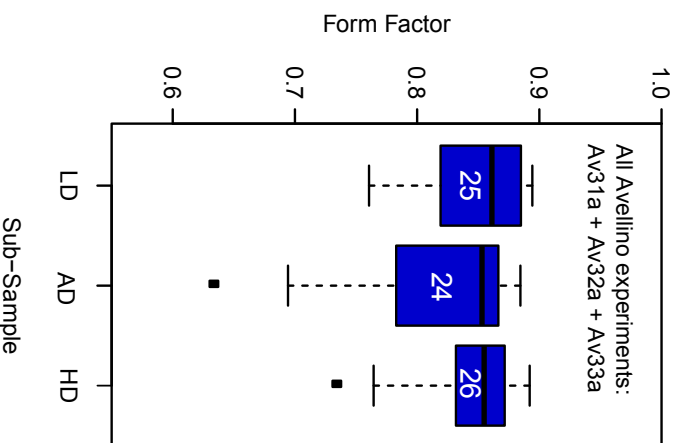
20mm  
e.g. Av33a HD

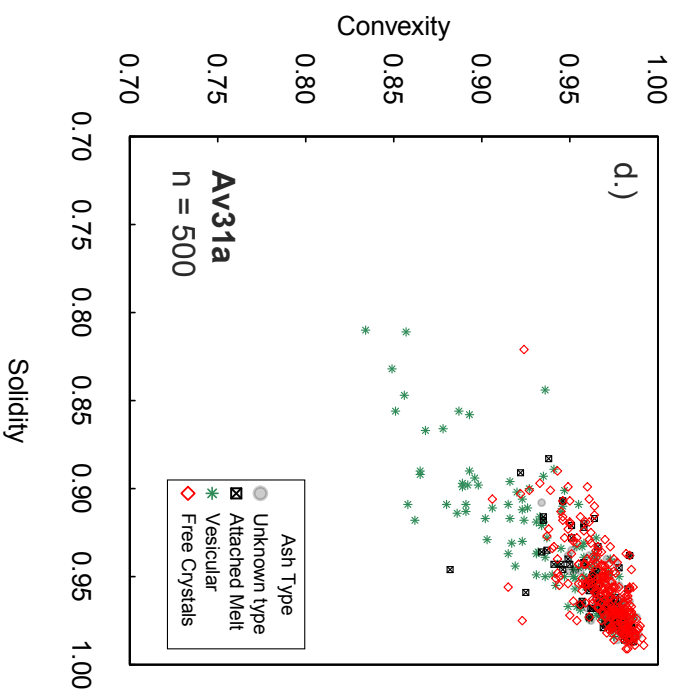
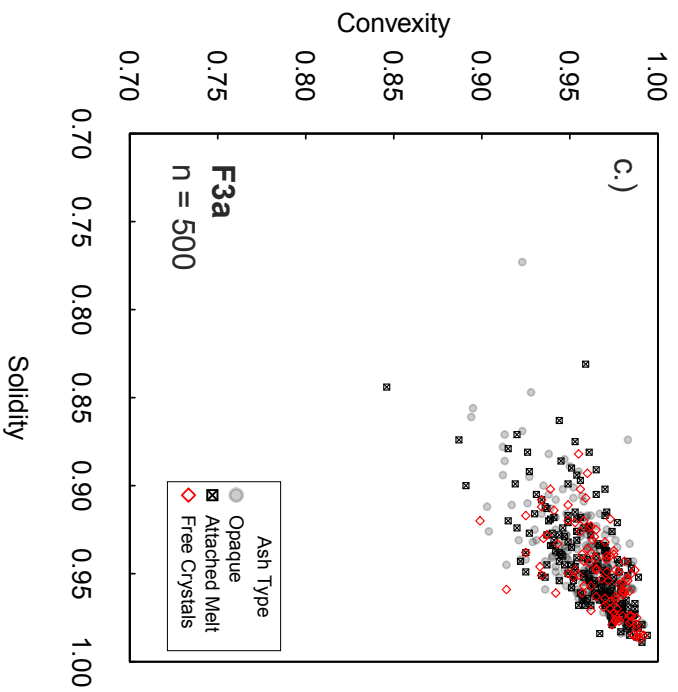
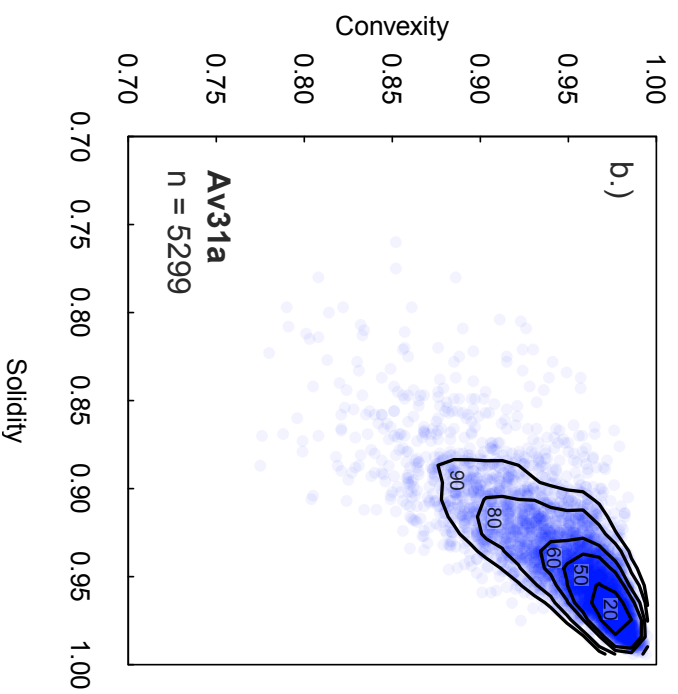
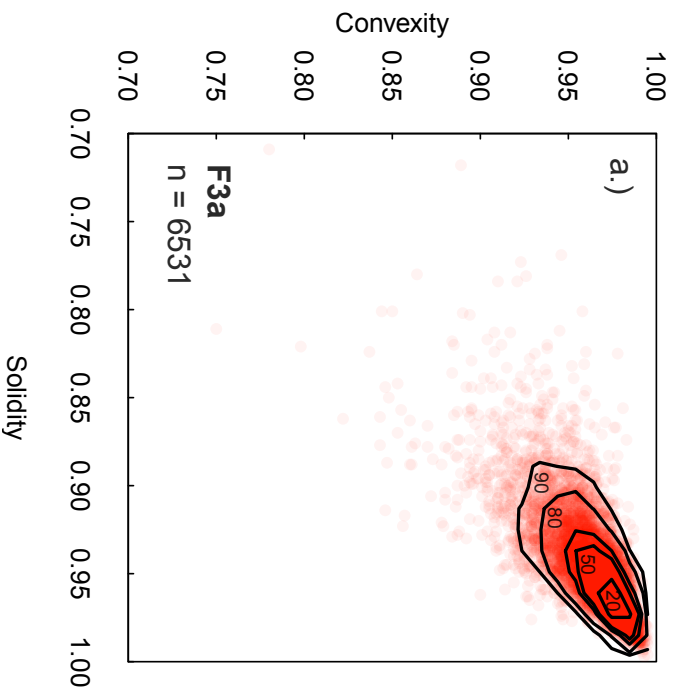


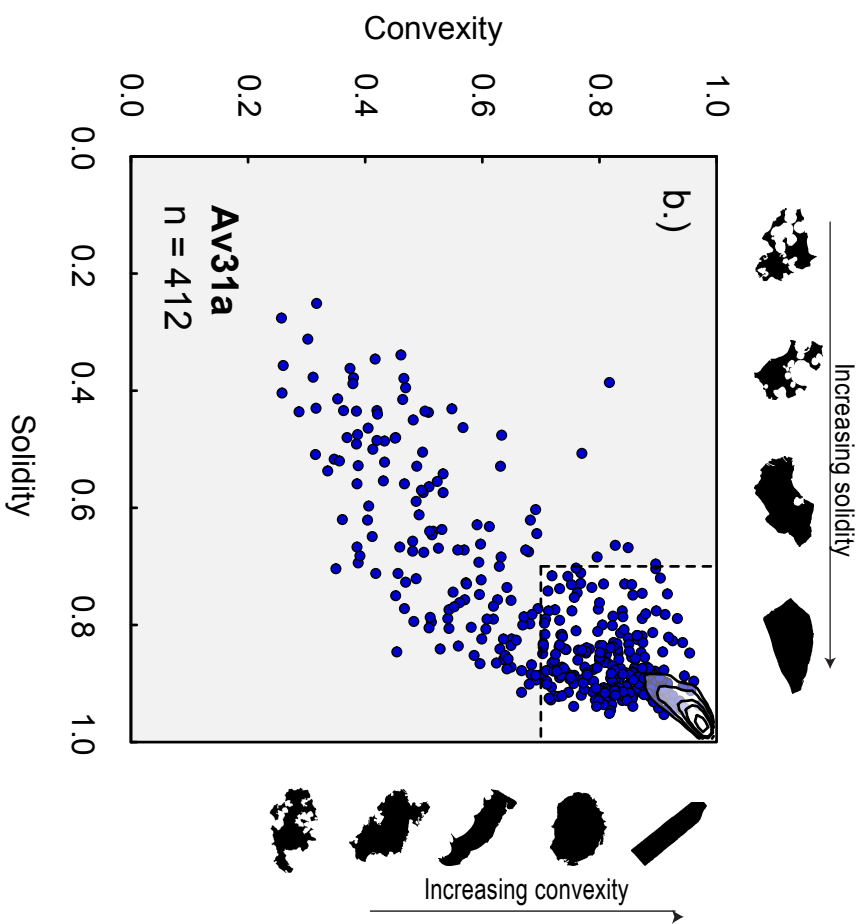
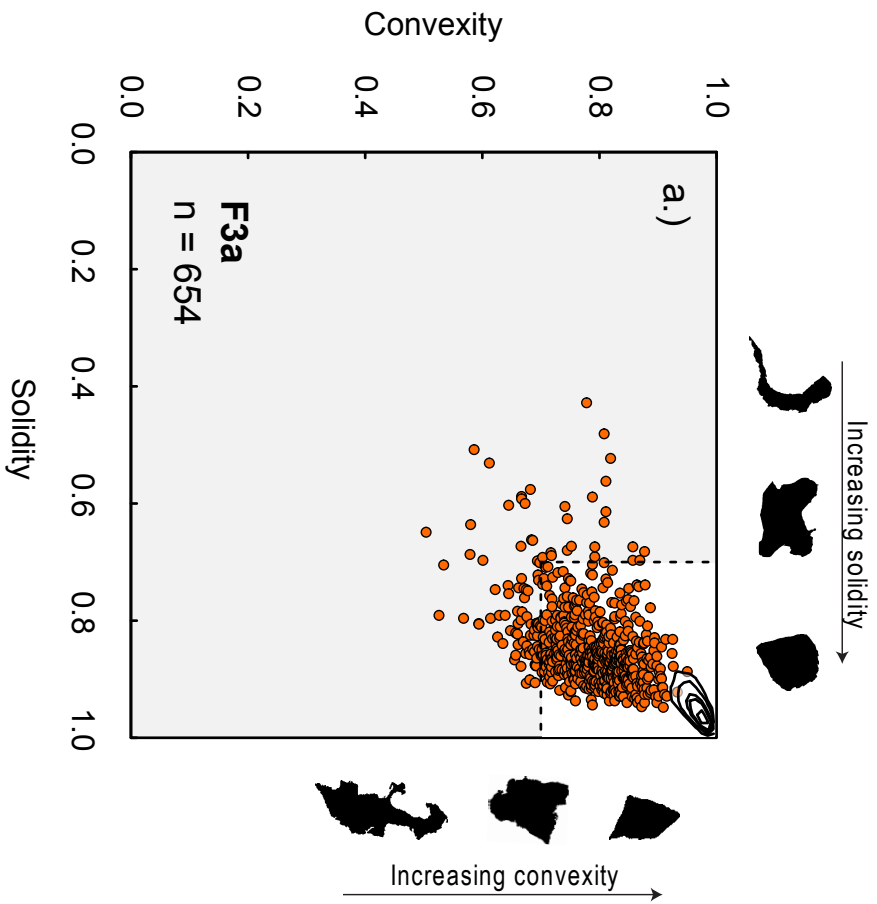
### Avellino After

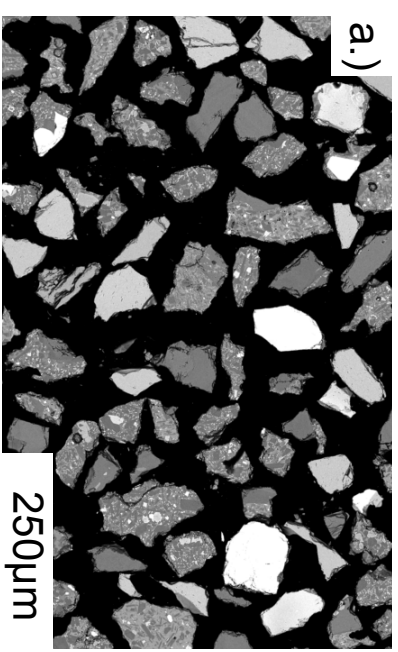
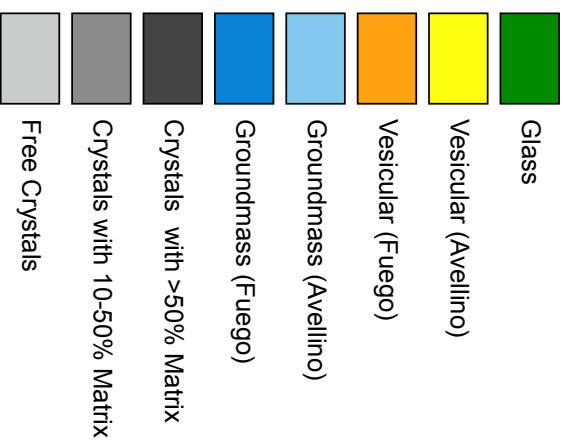
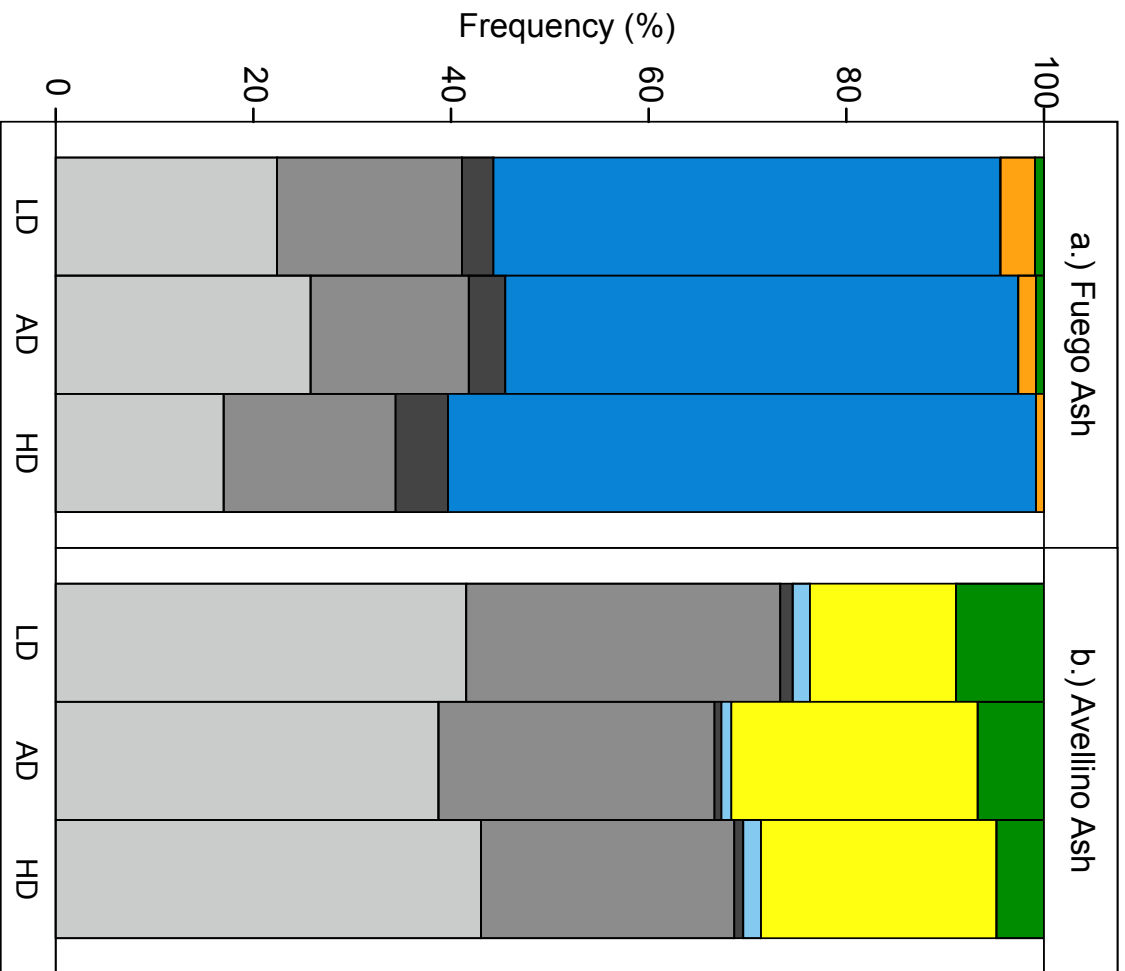
9 clasts

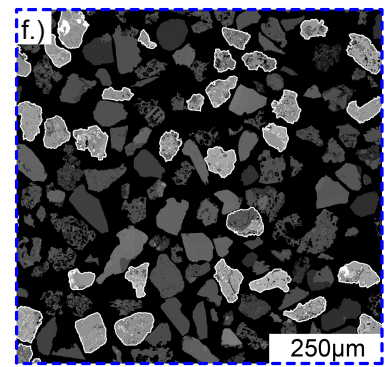
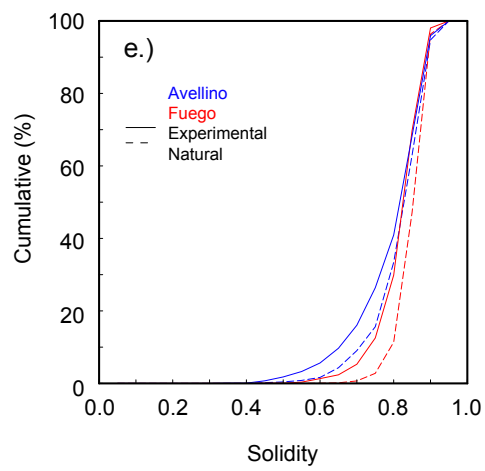
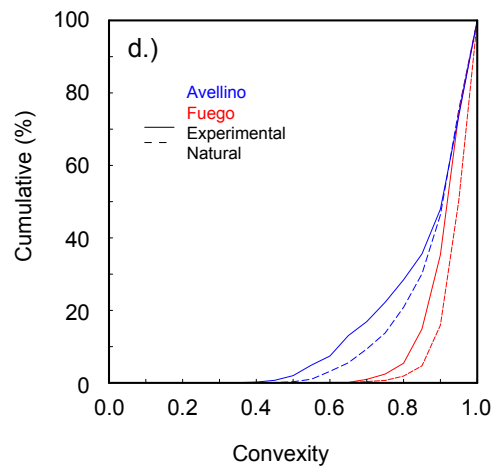
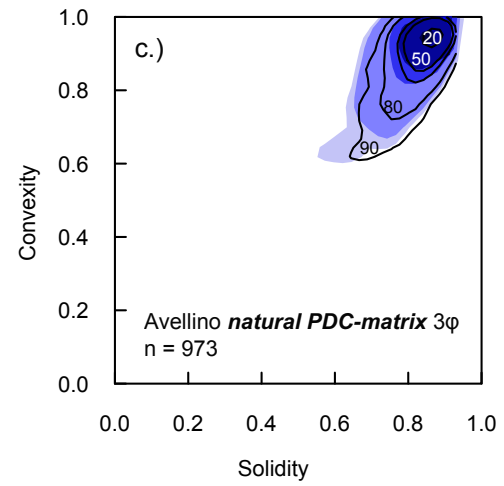
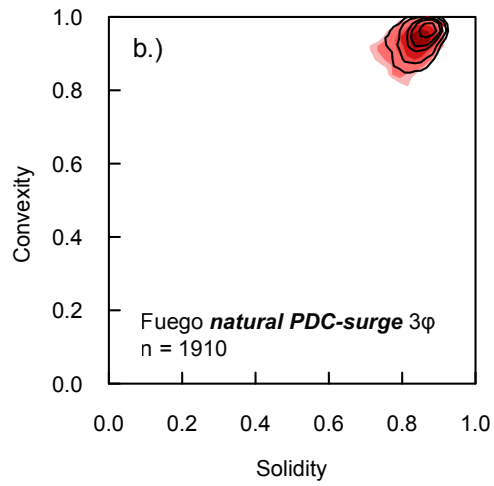
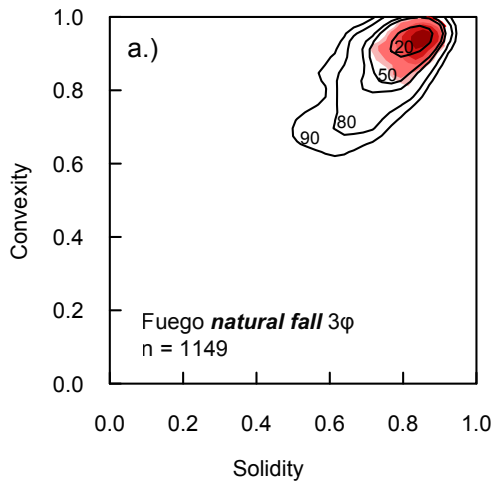
20mm  
e.g. Av33a HD











Natural PDC-matrix Avellino 3φ  
*large lithic component*

